The birth of a galaxy – III. Propelling reionisation with the faintest galaxies

John H. Wise[1]⋆, Vasiliy Demchenko[1], Martin Halicek[1], Michael L. Norman[2], Matthew J. Turk[3], Tom Abel[4], and Britton D. Smith[5]

[1] *Center for Relativistic Astrophysics, Georgia Institute of Technology, 837 State Street, Atlanta, GA 30332, USA*
[2] *Center for Astrophysics and Space Sciences, University of California at San Diego, La Jolla, CA 92093, USA*
[3] *Department of Astronomy, Columbia University, 538 West 120th Street, New York, NY 10027, USA*
[4] *Kavli Institute for Particle Astrophysics and Cosmology, Stanford University, Menlo Park, CA 94025, USA*
[5] *Institute of Astronomy, University of Edinburgh, Blackford Hill, Edinburgh EH9 3HJ, UK*

ABSTRACT

Starlight from galaxies play a pivotal role throughout the process of cosmic reionisation. We present the statistics of dwarf galaxy properties at $z > 7$ in haloes with masses up to $10^9 M_\odot$, using a cosmological radiation hydrodynamics simulation that follows their buildup starting with their Population III progenitors. We find that metal-enriched star formation is not restricted to atomic cooling ($T_{\rm vir} \geqslant 10^4$ K) haloes, but can occur in haloes down to masses $\sim 10^6 M_\odot$, especially in neutral regions. Even though these smallest galaxies only host up to $10^4 M_\odot$ of stars, they provide a significant fraction of the ionising photon budget because of their high number densities. We find that the galaxy luminosity function flattens above $M_{\rm UV} \sim -12$ with a number density that is unchanged during reionisation. The fraction of ionising radiation escaping into the intergalactic medium is inversely dependent on halo mass, decreasing from 50 to 5 per cent in the mass range $\log M/M_\odot = 7.0 - 8.5$. We find that low-mass galaxies are just as efficient at producing ionising photons per unit mass as atomic cooling haloes. However, they are gradually photo-suppressed as they are engulfed in ionised regions, giving way for larger galaxies to dominate the latter half of reionisation. Using our galaxy statistics in a semi-analytic reionisation model, we find a Thomson scattering optical depth consistent with the latest *Planck* results, while still being consistent with the UV emissivity constraints provided by Lyα forest observations at $z = 4 - 6$. We find that haloes less massive than the atomic cooling limit provide nearly 30 per cent to the total ionising photon budget. Our work suggests that an yet-to-be observed population of low-mass galaxies were responsible for starting reionisation at very high redshifts, which might be observed with JWST in surveys of gravitational lensed fields.

Key words: cosmology — methods: numerical — hydrodynamics — radiative transfer — star formation

1 INTRODUCTION

The process of cosmic reionisation is extended with H II regions growing around ionising sources that gradually coalesce, culuminating in an ionised universe by $z \sim 6$ (e.g. Gnedin & Ostriker 1997; Sokasian et al. 2003; Ciardi, Ferrara & White 2003; Furlanetto, Zaldarriaga & Hernquist 2004; Iliev et al. 2006; Robertson et al. 2010; Zahn et al. 2011; Trac & Gnedin 2011; So et al. 2013). However, there is still some tension between observational constraints on the timing and duration of reionisation. First, Lyα for-

est lines imply that the universe was mostly ionised by $z \sim 6$ (e.g. Gunn & Peterson 1965; Fan et al. 2002, 2006; Willott et al. 2007; Mortlock et al. 2011). Second, observations of the cosmic microwave background (CMB) from the *Wilkinson Microwave Anisotropy Probe (WMAP)* and *Planck* have measured the optical depth to Thomson scattering $\tau_e = 0.089^{+0.012}_{-0.014}$, which corresponds to the universe being $\sim$50 per cent ionised at $z = 11.1 \pm 1.1$ (Planck Collaboration et al. 2013). But the ionising emissivity measured at $z = 4 - 6$ through Lyα forest observations cannot account for this measured τ_e, indicating that the end of reionisation must be photon-starved (Bolton & Haehnelt 2007) and that the emissiv-

⋆ e-mail: jwise@physics.gatech.edu

ity must have been higher during reionisation. Third, the duration[1] of reionisation has been constrained to occur within $\Delta z < 7.9$ by measuring the kinetic Sunyaev-Zel'dovich effect with the *South Pole Telescope* (SPT; Zahn et al. 2012). These observations suggest that reionisation was an extended process, mainly occurring at $6 \lesssim z \lesssim 15$.

What population of ionising sources drives this global and extended transition? It is clear that quasars and the very brightest galaxies, which both are too rare, do not significantly contribute to the overall ionising photon budget of reionisation (e.g. Shapiro 1986; Dijkstra et al. 2004; Willott et al. 2010; Grissom, Ballantyne & Wise 2014). Starlight from galaxies are thought to provide the vast majority of the ionising photon budget from extrapolating the observed $z > 6$ galaxy luminosity function (LF) to low luminosities (e.g. Madau, Haardt & Rees 1999; Bouwens et al. 2012b; Haardt & Madau 2012; Shull et al. 2012; Robertson et al. 2013). Alternatively, massive, metal-free (Population III; Pop III) stars can contribute on the order of 10 per cent of the budget (Ricotti & Ostriker 2004a; Greif & Bromm 2006; Trac & Cen 2007; Wise & Abel 2008a; Ahn et al. 2012; Wise et al. 2012b; Paardekooper, Khochfar & Dalla Vecchia 2013; Johnson, Dalla & Khochfar 2013) because they are short-lived (e.g. Tumlinson & Shull 2000; Schaerer 2002) and can be suppressed by chemical enrichment and H_2-dissociating radiative feedback (e.g. Haiman, Rees & Loeb 1997; Haiman, Abel & Rees 2000; Machacek, Bryan & Abel 2001; Wise & Abel 2008b). Finally, X-ray radiation from X-ray binaries and accreting massive black holes partially ionise the intergalactic medium (IGM) and may contribute a non-negligible amount to the Thomson scattering optical depth (Ricotti & Ostriker 2004b; McQuinn 2012; Power et al. 2013; Fragos et al. 2013).

Deep galaxy surveys, such as the *Hubble Ultra Deep Field* (HUDF; Beckwith et al. 2006; Koekemoer et al. 2013) and CANDELS (Grogin et al. 2011; Koekemoer et al. 2011), can probe $z \gtrsim 6$ galaxies up to absolute UV magnitudes $M_{\rm UV} < -18$ or equivalently a stellar mass $M_\star \gtrsim 10^8 M_\odot$. Future deep surveys using the *James Webb Space Telescope (JWST)* and 30-m class ground-based telescopes will push this limit down to $M_{\rm UV} \sim -15.5$. At these high redshifts, the faint-end LF slope is steepening with redshift and is around -2 at $z \sim 8$ (e.g. Bouwens et al. 2011; Bradley et al. 2012; Oesch et al. 2012). The least massive galaxies can be suppressed through supernovae and/or radiative feedback, and this process should materialise as a flattening or turn-over in the LF, but starting at which limiting magnitude?

Any change in the LF behavior should be related to the star formation efficiency, i.e. $M_\star / M_{\rm gas}$, which is also connected to the effectiveness of gas cooling and the halo mass in principle. For instance, starting at the lowest mass haloes, the primary coolants in the interstellar medium (ISM) are molecular hydrogen and metals (e.g. C, O, Si), whereas above a virial temperature $T_{\rm vir} \sim 10^4$ K, they change to atomic hydrogen. Negative feedback in these small haloes are also a concern on whether they can sustain efficient star formation. Examples of such feedback include photo-evaporation, H_2 dissociation, and gas blowout from H II regions and SN, which all depend on halo mass (e.g. Gnedin 2000; Wise & Cen 2009; Stinson et al. 2013; Hopkins et al. 2013). In the H_2-cooling haloes with $M \sim 10^6 M_\odot$, H_2 can be dissociated by a moderate Lyman-Werner (LW; 11.2–13.6 eV) background. But in more massive haloes with $M \sim 10^7 M_\odot$, cold gaseous reservoirs can form even in the pres-

ence of a strong LW background (Wise & Abel 2007; Johnson, Greif & Bromm 2008; O'Shea & Norman 2008; Safranek-Shrader et al. 2012). Progressing up the mass scale, even atomic cooling haloes are prone to negative feedback; for example, haloes with masses $M \lesssim 2 \times 10^9 M_\odot$ can be photo-evaporated by an external radiation field, gradually boiling away their star-forming gas reservoir (Efstathiou 1992; Thoul & Weinberg 1996; Dijkstra et al. 2004; Shapiro, Iliev & Raga 2004; Okamoto, Gao & Theuns 2008; Finlator, Davé & Özel 2011).

How does the LF limiting magnitude $M_{\rm lim}$ affect reionisation histories? Recently, a few groups (Kuhlen & Faucher-Giguère 2012; Finkelstein et al. 2012; Robertson et al. 2013) have explored this question among other variations in their reionisation models. Kuhlen & Faucher-Giguère found a nearly linear dependence between τ_e and $M_{\rm lim}$, increasing τ_e from ~ 0.06 to 0.08 when $M_{\rm lim}$ increases from –13 to –10. Robertson et al. found little dependence on $M_{\rm lim}$ below –13. Whereas Finkelstein et al. showed that the escape fraction must be greater than 30 and 50 per cent to sustain reionisation at redshifts 6 and 7, respectively, if only the observed CANDELS galaxies contribute to the emissivity. Additional constaints on reionisation can be gained from the inferred ionising flux in the Lyα forest at $z = 4 - 6$ (Bolton & Haehnelt 2007; Kuhlen & Faucher-Giguère 2012). Extrapolating the LF down to $M_{\rm UV} = -13$ and assuming that the escape fraction $f_{\rm esc}$ is independent of halo mass, Finkelstein et al. also found that $f_{\rm esc} < 0.13$ is constrained by the measured ionising photon emissivity in Lyα forest observations at $z = 6$. It is clear from these studies that a population of unobserved dwarf galaxies are primarily responsible for driving cosmic reionisation.

To further refine reionisation models, it is pertinent to determine the characteristic properties of these unobserved dwarf galaxies. In particular, the stellar fraction, $M_\star / M_{\rm vir}$, and $f_{\rm esc}$ of high-redshift galaxies are the largest sources of uncertainty in reionisation models[2]. Current reionisation models favor scenarios that have a luminosity-weighted escape fraction that increases with redshift to match the observed τ_e value while being photon-starved at $z \sim 6$ (Alvarez, Finlator & Trenti 2012; Haardt & Madau 2012; Kuhlen & Faucher-Giguère 2012; Shull et al. 2012; Mitra, Ferrara & Choudhury 2013). For example, the model of Alvarez, Finlator & Trenti considers a scenario where galaxies in haloes of mass $10^8 \leqslant M/M_\odot \leqslant 2 \times 10^9$ with $f_{\rm esc} = 0.8$ dominate the ionising emissivity at early times and are gradually photo-suppressed (also see Sobacchi & Mesinger 2013). Then at $z \lesssim 6.5$, galaxies greater than $2 \times 10^9 M_\odot$ with lower escape fractions become sufficiently abundant to produce the majority of ionising photons, keeping the universe ionised in a photon-starved scenario.

The ionising escape fraction is a notoriously difficult quantity to measure both in high-redshift galaxy observations and theoretical studies. Nevertheless, this topic has been a subject of great interest to constrain the reionisation history of the universe. On the observational side, it is nearly impossible to detect Lyman continuum (LyC) emission at $z > 4$ because the number density of Lyman limit systems rapidly increases with redshift (Inoue & Iwata 2008). However at $z \sim 3$ when the IGM optical depth is around unity, detection of intrinsic LyC radiation becomes feasible. Deep narrow-band galaxy imaging and spectroscopy have uncovered LyC emission in 10–20 per cent of Lyman-break galaxies, which can be in-

---

[1] Zahn et al. (2012) defines Δz as the redshift elapsed between 20 and 99 per cent ionised.

[2] Other properties that could affect the ionising emissivity originating from such galaxies are the gas fraction, initial mass function (IMF), gaseous and stellar morphology, and the strength and duration of star formation events.

terpreted as the mean ionising radiation escape fraction (Steidel, Pettini & Adelberger 2001; Shapley et al. 2006; Iwata et al. 2009; Nestor et al. 2011; Vanzella et al. 2012; Jones et al. 2013).

Theoretical efforts have focused on the calculation of f_{esc} for over a decade, using analytical and numerical techniques with varying model complexities. The galaxies studied in these cumulative works span over six orders of magnitude in halo mass and are considered out to $z = 15$. Models of the escape fraction found that $f_{esc} \lesssim 0.06$ for Milky Way like galaxies (Dove, Shull & Ferrara 2000), and, in general, it depends on the density structure of the ISM and star formation rate (SFR; Ciardi, Bianchi & Ferrara 2002; Clarke & Oey 2002; Wise & Cen 2009; Fernandez & Shull 2011; Benson, Venkatesan & Shull 2013). At high redshift, Ricotti & Shull (2000) found that higher escape fractions of $f_{esc} \gtrsim 0.1$ in haloes with masses $M \leqslant 10^7 M_\odot$, but they posed the valid question of whether these low-mass haloes can host star formation. This paper will address this exact question, utilising a cosmological radiation hydrodynamics simulation of dwarf galaxy formation.

Conversely, because of the higher mean densities at high redshift, Wood & Loeb (2000) argued that $f_{esc} \leqslant 0.01$, and Fujita et al. (2003) found that $f_{esc} \leqslant 0.1$ from disks of dwarf starburst galaxies with total masses between 10^8 and $10^{10} M_\odot$. Paardekooper et al. (2011) found similar results for isolated high-redshift disk galaxies with total masses of 10^8 and $10^9 M_\odot$. All of the aforementioned models were idealised calculations of isolated galaxies; however Razoumov & Sommer-Larsen (2006, 2007) and Gnedin, Kravtsov & Chen (2008) used cosmological simulations of galaxy formation with radiative transfer to conclude that $f_{esc} = 0.01 - 0.1$ and $f_{esc} \sim 0.01 - 0.03$, respectively, in haloes with $M \geqslant 10^{11} M_\odot$ at $z = 3-5$. If these low escape fractions were present in lower mass galaxies before reionisation, insufficient LyC emission would escape from them to reionise the universe by $z = 6$ (Gnedin 2008).

In radiation hydrodynamics simulations of isolated dwarf irregular galaxies at $z = 8$, Wise & Cen (2009) found that $f_{esc} \gtrsim 0.3$, which was confirmed by several other groups with numerical simulations shortly afterward (Razoumov & Sommer-Larsen 2010; Yajima, Choi & Nagamine 2011; Paardekooper, Khochfar & Dalla Vecchia 2013; Ferrara & Loeb 2013). These works imparted momentum to the idea that protogalaxies could be the dominant driver of reionisation, as originally proposed by Ricotti & Shull (2000). Semi-analytic models of reionisation tested these ideas and further constrained the required escape fraction in high-redshift dwarf galaxies to be increasing with redshift, suggesting that low-mass galaxies with high f_{esc} contributed a significant amount of the ionising photon budget (Haardt & Madau 2012; Alvarez, Finlator & Trenti 2012; Mitra, Ferrara & Choudhury 2013).

Unfortunately, not even *JWST* has the capability to directly detect the lowest-luminosity galaxies that could provide the majority of ionising photons during the earlier epochs of reionisation. Comparisons to local dwarf galaxies can be made, but in principle, similarities could be few because some form in a neutral and cool environment, largely unaffected by the ensuing inhomogeneous reionisation. In addition, some are directly affected by radiative and supernova feedback from Pop III stars (Johnson & Bromm 2006; Wise & Abel 2008b; Greif et al. 2010; Maio et al. 2010; Wise et al. 2012b; Pawlik, Milosavljević & Bromm 2013; Muratov et al. 2013). Thus for the time being, this problem is best approached theoretically.

This paper focuses on these early dwarf galaxies that are sensitive to feedback effects in haloes with $M \lesssim 10^9 M_\odot$. The primary goal of this paper is to quantify the mean stellar and gaseous properties, the ionising escape fractions, and LFs of high-redshift dwarf galaxies, and their contribution to global reionisation. In the next section, we outline our simulation set-up and methods. Then, in Section 3, we present scaling relations for stellar mass, gaseous fractions, intrinsic UV magnitudes, and ionising escape fractions of the simulated dwarf galaxies. Next, in Section 4, we apply our mean scaling relations to a semi-analytic reionisation model and show the resulting reionisation history when low-luminosity galaxies are considered. We discuss the implications of our results and possible observational signatures of the first galaxies in Section 5, where we also compare our results to previous studies. Lastly, we summarise our findings in Section 6.

2 METHODS

We further analyze the "RP" simulation originally presented in Wise et al. (2012a, hereafter W12), which focused the role of radiation pressure during dwarf galaxy formation. In this paper, we will focus on the LF, escape fraction of UV radiation, and the role of these first galaxies during reionisation. A detailed description of the radiative cooling, star formation, and stellar feedback models is given in W12, thus we only briefly describe the input physics and methods in this section.

2.1 Simulation setup

This simulation was run with the adaptive mesh refinement (AMR) code ENZO v2.0[3] (The Enzo Collaboration et al. 2013). It uses an N-body adaptive particle-mesh solver (Efstathiou et al. 1985; Couchman 1991; Bryan & Norman 1997) to follow the DM dynamics. It solves the hydrodynamics equations using the second-order accurate piecewise parabolic method (Woodward & Colella 1984; Bryan et al. 1995), while an HLLC Riemann solver ensures accurate shock capturing with minimal viscosity. We use the nine-species (H I, H II, He I, He II, He III, e$^-$, H$_2$, H$_2^+$, H$^-$) non-equilibrium chemistry model in ENZO (Abel et al. 1997; Anninos et al. 1997) and the H$_2$ cooling rates from Glover & Abel (2008). In addition to the primordial radiative cooling, we include metal and molecular line cooling, using cooling rates that are calculated with CLOUDY (Smith, Sigurdsson & Abel 2008).

We initialise a simulation of 1 Mpc on a side at $z = 130$ with a base resolution of 256^3, using GRAFIC (Bertschinger 2001) with the 7-year *WMAP* ΛCDM+SZ+LENS best fit (Komatsu et al. 2011): $\Omega_M = 0.266$, $\Omega_\Lambda = 0.734$, $\Omega_b = 0.0449$, $h = 0.71$, $\sigma_8 = 0.81$, and $n = 0.963$ with the variables having their usual definitions. The DM mass resolution is 1840 $M_\odot$, and the maximum spatial resolution is 1.0 comoving pc or 12 levels of AMR refinement. We refine the grid on baryon overdensities of $3 \times 2^{-0.2l}$, where l is the AMR level. We also refine on a DM overdensity of three and always resolve the local Jeans length by at lease four cells, avoiding artificial fragmentation during gaseous collapses (Truelove et al. 1997). If any of these criteria are met in a single cell, it is flagged for further spatial refinement. We stop the simulation at $z = 7.3$ when the simulation box is 70 per cent ionised by volume, and the ray tracing from ~ 1000 point sources becomes computationally expensive in the optically thin regime. We analyze the simulation from outputs that are written 12.5 Myr apart until $z = 8$ and then every 1 Myr until the ending redshift.

---

[3] enzo-project.org, changeset 03a72f4f189a

2.2 Star formation and feedback

We use distinct star formation and feedback models for Population II and III with the latter forming when the gas metallicity of the star forming gas is below $10^{-4}\,Z_\odot$. The star formation criteria are similar to the original Cen & Ostriker (1992) model but with a critical H_2 fraction for Population III star formation, and for Population II stars, the model has been modified to allow for star-forming clouds that are Jeans resolved. We model the formation, main sequence, and stellar endpoints of these populations with the following characteristics:

• **Population II:** Each star particle represents a stellar cluster with a minimum mass $M_{min} = 1000\,M_\odot$ and a Salpeter IMF. The initial accretion event converts 7 per cent of the cold ($T < 1000$ K) gas within a sphere with a dynamical time of 3 Myr ($\bar{\rho} \simeq 1000\mu\,cm^{-3}$) into a star particle (see W12). If the initial star particle is less than $1000\,M_\odot$, then the star particle continues to accrete until it reaches this threshold. In the case where it does not reach M_{min} within a dynamical time of 3 Myr, the accretion halts at this point. Star particles only emit radiation after this accretion phase is completed. They emit 6000 hydrogen ionising photons per stellar baryon over a lifetime of 20 Myr. We consider a monochromatic spectrum with an energy of 21.6 eV (Schaerer 2003). After living for 4 Myr, they generate 6.8×10^{48} erg s^{-1} $M_\odot^{-1}$ in supernovae that are injected into resolved spheres of radius 10 pc.

• **Population III:** Each star particle represents a single star whose mass is randomly drawn from a Salpeter IMF that exponentially decays below a characteristic mass $M_{char} = 100 M_\odot$,

$$f(\log M)dM = M^{-1.3} \exp\left[-\left(\frac{M_{char}}{M}\right)^{1.6}\right] dM. \qquad (1)$$

The main-dependent hydrogen ionising and Lyman-Werner photon luminosities and lifetimes are taken from Schaerer (2002). We consider a monochromatic spectrum with an energy of 29.6 eV, appropriate for the near-constant 10^5 K surface temperatures of Pop III stars. The supernova explosion energies and metal ejecta masses from Nomoto et al. (2006) and Heger et al. (2003) are used for Type II (20–40 $M_\odot$) and pair instability SNe (140–260 $M_\odot$), respectively.

The hydrogen ionising radiation emitted during main sequence are propagated with adaptive ray tracing (Abel & Wandelt 2002; Wise & Abel 2011) that is based on the HEALPix framework (Górski et al. 2005). The radiation field is evolved at every hydrodynamics timestep of the finest AMR level that is on the order of 10 kyr. The photo-heating that occurs on these timesteps couples the radiation effects to the hydrodynamics. In addition, this simulation considers the momentum transfer from ionising radiation to the absorbing gas, i.e. radiation pressure. We model the LW radiation with a time-dependent optically-thin soft UV background and add inverse square profiles, centred on all Pop II and III star particles, to estimate the total LW radiation at all points. Using this physics set, we have shown in W12 that the galaxies produced in this simulation match the luminosity-metallicity relation for local dwarf galaxies and does not suffer from the well-known galaxy overcooling problem seen in many previous galaxy formation simulations.
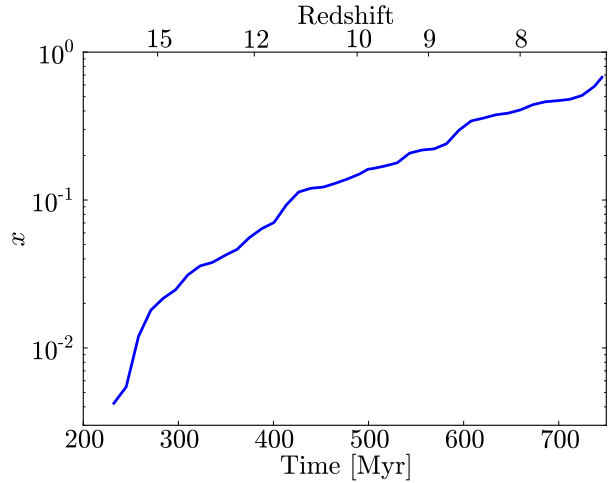

Figure 1. Ionisation history of the simulation, showing the ionised volume fraction x. We consider a computational element to be ionised if $x \geqslant 0.5$. Reionisation in the simulation starts when the first Pop III stars form in the calculation at $z = 17$.

3 SIMULATION RESULTS

The previous two papers in this series studied the individual properties of selected galaxies[4]. In this work, we study the global statistics of galaxies, in particular, their stellar masses, SFRs, gas fractions, LF, the fraction of escaping UV radiation, and their contribution to reionisation. The stellar radiation from these galaxies reionise 70 per cent of the simulation volume by $z = 7.3$, and the ionisation history is shown in Figure 1. It should be noted that this history is not cosmologically representative as a simulation box of $\gtrsim 100$ Mpc/h is required (e.g. Iliev et al. 2006, 2013) for such a study. However the SFRs and UV escape fractions are important to quantify in a small volume, high-resolution simulation, so they can guide radiation source models in large volume reionisation calculations needed for predictions for a cosmic reionisation history.

3.1 Dwarf galaxy properties

It has generally been thought that the galaxies begin to form in haloes that can support hydrogen atomic cooling with $T_{vir} \gtrsim 10^4$ K because molecular hydrogen is easily dissociated when the halo is exposed to a UV background. However, previous numerical studies have shown that H_2 formation and radiative cooling occurs in lower mass haloes, even in the presence of a strong Lyman-Werner (LW) background (Wise & Abel 2007; O'Shea & Norman 2008). In addition if the halo is chemically enriched, then metal-line radiative cooling adds to the likelihood that the halo will collapse and form stars. At the ending redshift $z = 7.3$ of our simulation, there are 32 haloes that host metal-enriched star formation. The smallest such halo has a virial mass $M_{vir} = 7.6 \times 10^5 M_\odot$ and stellar mass $M_\star = 840 M_\odot$, which has been enriched by a nearby supernova and did not form any Population III stars. The largest halo has $M_{vir} = 6.8 \times 10^8 M_\odot$ and $M_\star = 3.7 \times 10^6 M_\odot$. Here we define the halo as a sphere that contains an overdensity of $18\pi^2$ relative to the critical density.

---

[4] We define a galaxy as any metal-enriched stellar system that is gravitationally bound and exists in a dark matter halo (Willman & Strader 2012).

Table 1. General galaxy and host halo properties

$\log M_{\rm vir}$ $[M_\odot]$ (1)	$\log M_\star$ $[M_\odot]$ (2)	$\langle f_{\rm host}\rangle$ (3)	$\log f_\star$ (4)	$f_{\rm gas}$ (5)	$M_{\rm UV}$ (6)	$\log L_{\rm bol}$ $[L_\odot]$ (7)	$\log \dot{N}_{\rm ion}$ $[{\rm ph\ s^{-1}}]$ (8)
6.5	$3.41^{+0.10}_{-0.06}$	2.4×10^{-4}	$-1.88^{+0.35}_{-0.43}$	$0.05^{+0.02}_{-0.03}$	$-5.61^{+0.73}_{-0.86}$	$4.81^{+0.20}_{-0.31}$	$49.2^{+0.1}_{-0.2}$
7.0	$3.59^{+0.24}_{-0.33}$	0.052	$-2.25^{+0.11}_{-0.50}$	$0.06^{+0.02}_{-0.03}$	$-6.09^{+1.35}_{-0.93}$	$5.02^{+0.26}_{-0.55}$	$49.5^{+0.2}_{-0.1}$
7.5	$3.88^{+0.18}_{-0.29}$	0.28	$-2.48^{+0.27}_{-0.32}$	$0.07^{+0.01}_{-0.02}$	$-7.17^{+1.30}_{-1.22}$	$5.43^{+0.42}_{-0.50}$	$49.6^{+0.3}_{-0.4}$
8.0	$4.60^{+0.30}_{-0.12}$	0.90	$-2.25^{+0.15}_{-0.04}$	$0.10^{+0.02}_{-0.02}$	$-9.59^{+0.87}_{-0.95}$	$6.39^{+0.39}_{-0.39}$	$49.9^{+0.3}_{-0.3}$
8.5	$5.74^{+0.31}_{-0.37}$	1.0	$-1.80^{+0.23}_{-0.21}$	$0.13^{+0.00}_{-0.00}$	$-13.72^{+0.82}_{-0.72}$	$8.06^{+0.26}_{-0.31}$	$51.6^{+0.1}_{-0.1}$

Notes: Statistics are shown for galaxies at all times in 0.5 dex bins in $M_{\rm vir}$. Column (1): Virial mass. Column (2): Stellar mass. Column (3): Time-averaged galaxy occupation fraction of halos. See Figure 2 for the time dependent of this fraction. Column (4): Star formation efficiency, $M_\star/M_{\rm gas}$. Column (5): Gas mass fraction. Column (6): UV magnitude at 1500 Å. Column (7): Bolometric luminosity. Column (8): Ionizing photon luminosity from young (< 20 Myr) stars. Errors shown are 1-σ deviations.
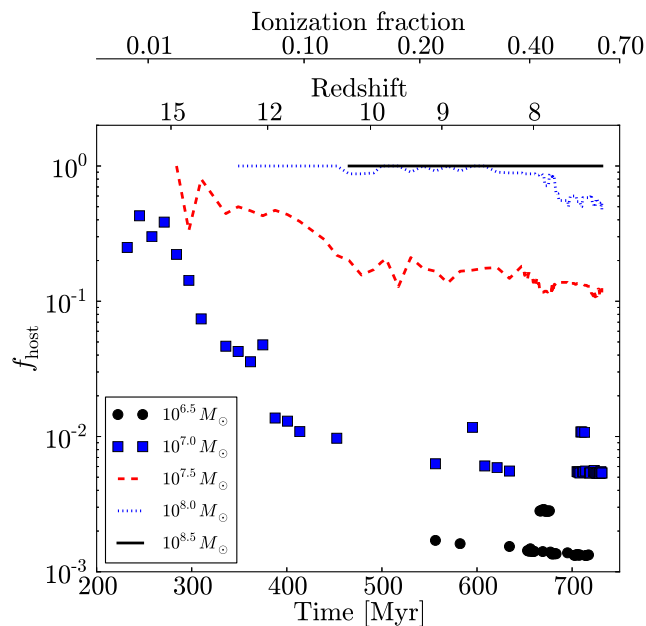

Figure 2. The fraction of haloes that host a metal-enriched stars as a function of time in five different mass bins. The corresponding ionization fraction is shown on the upper axis. See Figure 1 for a plot of ionization history. Star formation in the non-atomic cooling haloes ($M_{\rm vir} < 10^8 M_\odot$) occurs at high-redshift, only to be suppressed by external radiative feedback.

There exists a wide range of stellar and gaseous mass fractions between these extremes. Because these low-mass haloes are heavily affected by stellar feedback, they cycle between quiescence and star-forming phases during their histories (Wise et al. 2012b). To capture the whole range of halo and galaxy properties from our small set of simulated dwarf galaxies, we present our results from *all redshifts* until the final redshift. During inhomogeneous reionization, we have found that H_2-cooling halo properties are more dependent on environment (i.e. neutral or ionised) instead of halo mass. Figure 2 illustrates the evolution of galaxy occupation fraction $f_{\rm host}$, i.e. haloes that host metal-enriched stars, that is divided into five different mass bins with a width of 0.5 dex. The time-averaged values of $f_{\rm host}$ are shown in Table 1. Because the galaxy formation suppression shown in Figure 2 is dependent on the particular reionization history of this simulation, the ionization fraction x

and not the exact redshifts in this small box simulation, the values of x should be used when applying these data.

At the low-mass range at early times, galaxies form in about one-third of the haloes with $M_{\rm vir} = 10^7 M_\odot$, and this fraction steeply decreases after $z \sim 15$ ($x \sim 0.02$) to one per cent within a halo sound crossing time $t_{\rm sc} \sim 100$ Myr (Shapiro, Iliev & Raga 2004). These low-mass galaxies are some of the first to form in the simulation and ionise the surrounding IGM. The subsequent suppression occurs because the haloes must then accrete from a preheated IGM. The filtering mass,

$$M_{\rm F}^{2/3}(a) = \frac{3}{a}\int_0^a da'\, M_{\rm J}^{2/3}(a')\left(1 - \frac{a'}{a}\right), \qquad (2)$$

is an analytical measure of the minimum mass of a Jeans-unstable halo in such a situation. Here a and $M_{\rm J}$ are the scale factor and time-dependent Jeans mass of the accreted gas (Gnedin & Hui 1998; Gnedin 2000). The Jeans mass in the ionised regions is approximately $4 \times 10^8 M_\odot$ at $z = 20$ and increases to $10^9 M_\odot$ by $z = 7$ for a gas at the mean baryon density and $T = 10^4$ K. The filtering mass correspondingly increases from $10^7 M_\odot$ at $z = 15$ to $10^8 M_\odot$ at $z = 7$ (see Wise et al. 2012b). Similar but not as severe suppression occurs at $M_{\rm vir} = 10^{7.5} M_\odot$ in which $f_{\rm host}$ is around 0.5 at $z \gtrsim 12$ ($x \sim 0.1$) and decreases to ~ 0.15 afterwards. This remaining 15 per cent of galaxies are not actively forming stars, but they host stars that formed in their initial star formation event and have not accreted additional mass. Atomic cooling haloes with $M_{\rm vir} \geqslant 10^8 M_\odot$ all host galaxies at $z \geqslant 8$. After this time, star formation in half of the $M_{\rm vir} = 10^8 M_\odot$ haloes is suppressed because the filtering mass is now $\sim 10^8 M_\odot$.

Although mass accretion and star formation histories differ from halo to halo, the stellar and gaseous properties exhibit general trends with respect to halo mass with some inter-halo variations. Figure 3 shows the time-averaged stellar masses $M_\star$, SFRs, star formation efficiencies $f_\star = M_\star/M_{\rm gas}$, gas fraction $f_{\rm gas} = M_{\rm gas}/M_{\rm vir}$, bolometric luminosity $L_{\rm bol}$, and AB magnitude $M_{\rm UV}$ at 1500Å of all of the galaxies as a function of halo mass. We calculate $L_{\rm bol}$ and $M_{\rm UV}$ using the stellar population synthesis model GALAXEV (Bruzual & Charlot 2003), using the star particle ages, masses, and metallicities as input into GALAXEV and assuming an instantaneous burst model for each star particle. We do not consider any nebular emission. The shaded regions in the figure show the probability density function (PDF) that is weighted by the time between outputs (see §2.1) and is normalised in each column. The points show the average values and 1-σ deviations in bins of 0.5 dex, which are also shown in Table 1.
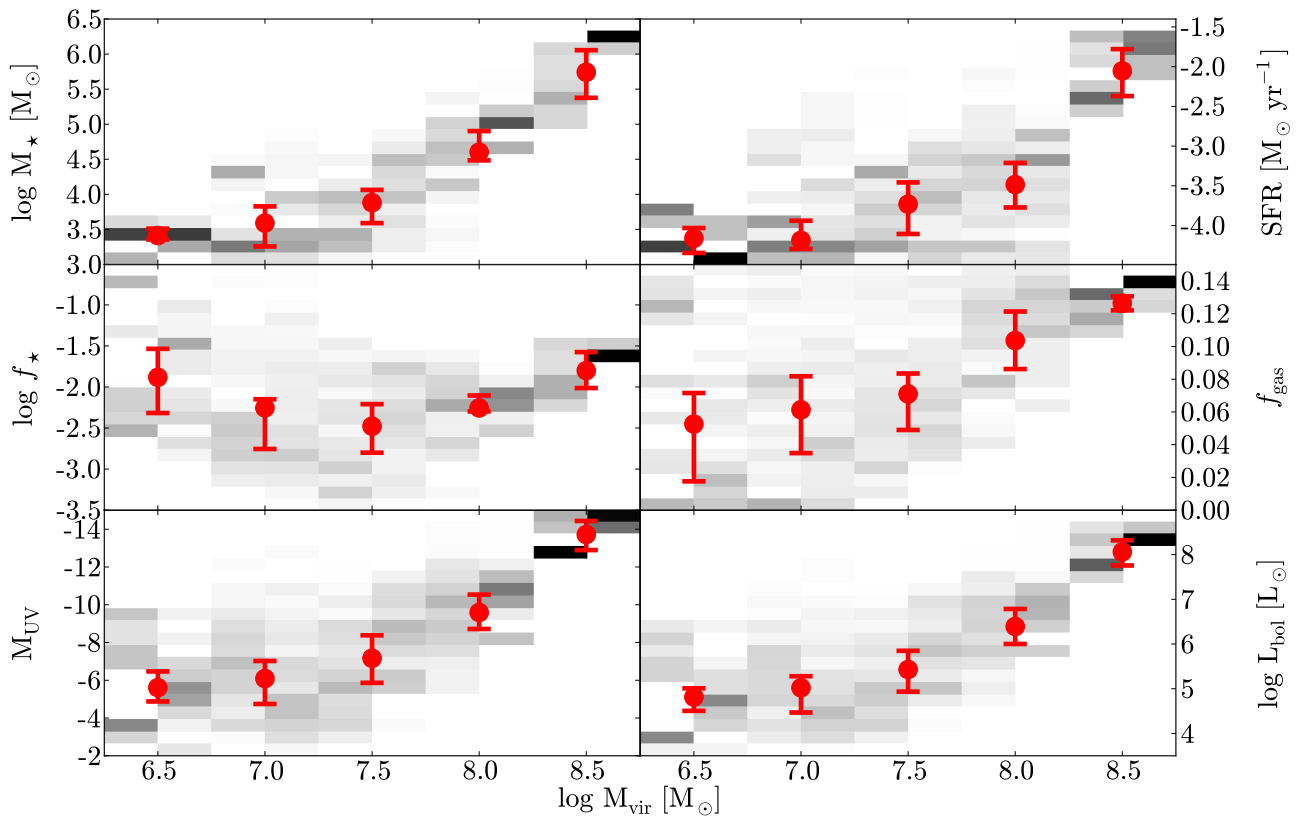
Figure 3. (*Clockwise from the upper left*) Stellar mass, star formation rate, gas mass fraction, bolometric stellar luminosity, absolute UV magnitude at 1500 Å from the stellar component, and star formation efficiency of all star-forming haloes at all redshifts. The pixels show the probability distribution function that is weighted by the time between snapshots. The points and error bars show the mean values and standard deviations in 0.5 dex bins, respectively. The increase in SFRs and luminosities at $10^8 M_\odot$ are caused by higher gas fractions and more efficient radiative cooling through atomic hydrogen line transitions. Below this mass scale, star formation is induced primarily through metal fine-structure line and H_2 cooling.

The stellar mass and SFRs in H_2-cooling haloes exhibit less of a dependence on halo mass than atomic cooling haloes with $M_\star$ increasing from $10^{3.4}$ to $10^{3.9} M_\odot$ over a halo mass range $\log M_{\rm vir} = [6.5, 7.5]$. In comparison, $M_\star$ increases by almost two orders of magnitude over the next decade of halo mass. Correspondingly, similar behaviour is seen in their SFRs, absolute UV magnitudes, and bolometric luminosities. What causes this change in behaviour? We can gain some insight by exploring how $f_{\rm gas}$ and $f_\star$ vary with halo mass. We see that the average value of $f_\star$ only varies by a factor of three around 0.01 over the entire mass range with a minimum at $M_{\rm vir} = 10^{7.5} M_\odot$. This concavity in $f_\star$ is caused after the galaxy experiences its first Pop II star formation event, whose feedback suppresses any further star formation until the gas reservoir is replenished. During this suppression phase and after the outflows have ceased, the halo gas mass increases as the stellar mass remaining constant, leading to a decrease in $f_\star$ as shown in the plot. Furthermore, once the halo can cool through atomic line transitions, the star formation efficiency increases. On the other hand, the average value of $f_{\rm gas}$ steadily increases from 0.05 at $M_{\rm vir} = 10^{6.5} M_\odot$ up to 0.13 in $10^{8.5} M_\odot$ haloes. The larger scatter in low mass haloes originates from their susceptibility to internal and external radiative and supernova feedback. Varying degrees of feedback are caused by environment and differing Pop III stellar masses that their progenitors hosted. At $M_{\rm vir} > 10^8 M_\odot$, the gravitational potential well is deep enough so that the outflows only contain a small mass fraction. Thus, we conclude that both

Table 2. Mean dwarf galaxy luminosity function at $M_{\rm UV} > -12$

Redshift	ϕ [mag^{-1}Mpc^{-3}]
7.3	2.7 ± 1.5
8	2.5 ± 1.5
9	2.9 ± 1.5
10	2.1 ± 1.1
12	2.2 ± 1.2
15	1.9 ± 0.7

the increase in the star formation efficiency and gas mass fraction cause the greater star formation rates as haloes transition from H_2-cooling to atomic line cooling.

3.2 Luminosity functions

We have shown that galaxies begin to form in haloes that rely on H_2 and metal-line cooling but not atomic line cooling. Recall that these haloes can have masses below the filtering mass. During this phase, star formation is less efficient than larger haloes with $T \gtrsim 10^4$ K. Afterward, they transition to more efficient star formation in atomic cooling haloes, which can be gradual or sudden if a galaxy experiences a major merger or not, respectively. These two different modes of galaxy formation should manifest in the galaxy luminosity function at high ($M_{\rm UV} \gtrsim -15$) magnitudes.

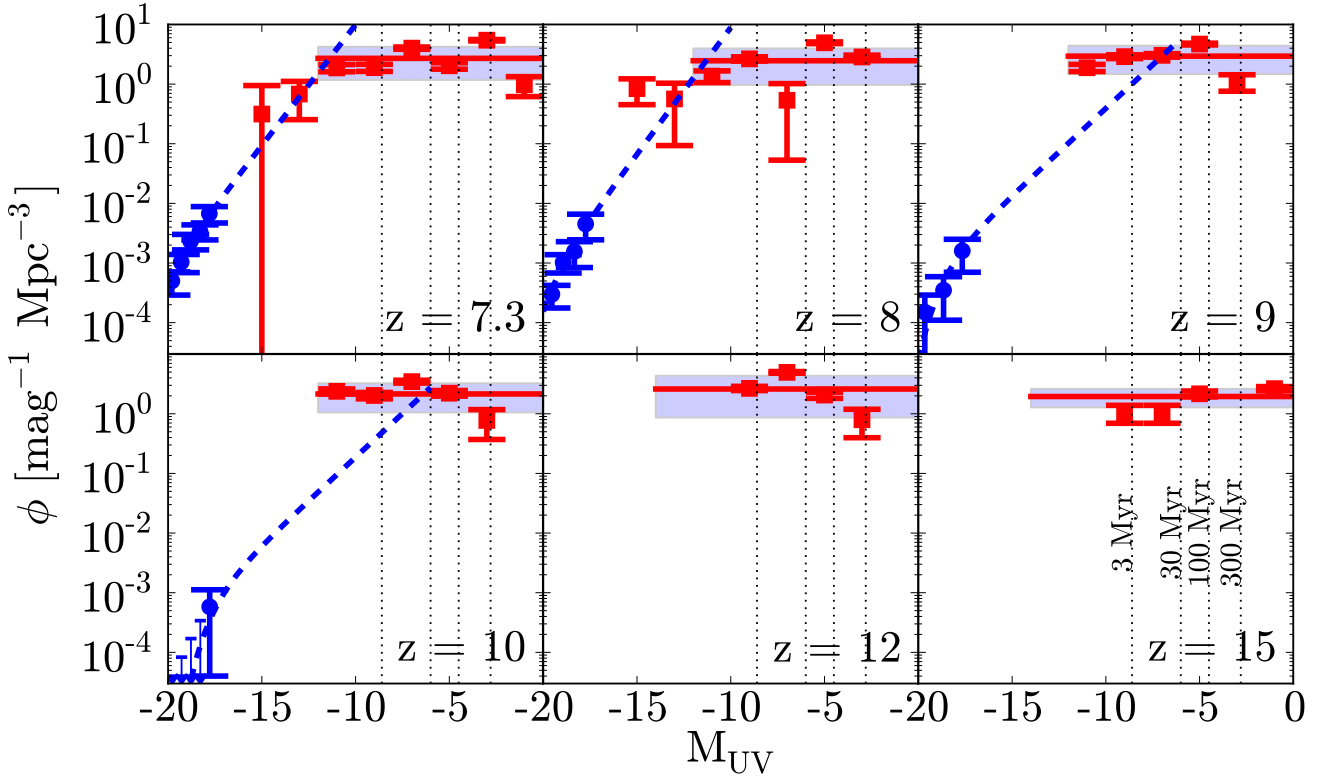Before constructing LFs from our data, we first check whether

Figure 5. Galaxy LFs from the simulation (red squares) and the Hubble Ultra Deep Field (blue circles) at redshifts 7, 8, 9, 10, 12, and 15. The blue dashed line shows the fits from Bouwens et al. (2011) for the redshift 7 and 8 data and Oesch et al. (2013) for the redshift 9 and 10 data. The red solid line and surrounding shaded region shows the average number density and standard deviation of galaxies with $M_{UV} > -12$. The vertical dotted lines show the UV magnitude of one star particle at our resolution limit of $M_\star = 1000 M_\odot$ at various ages.
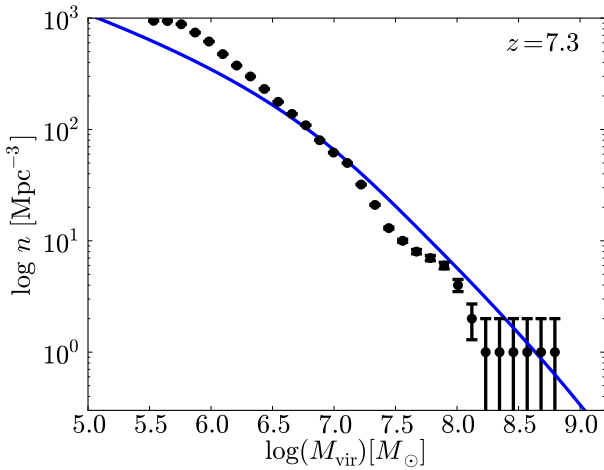

Figure 4. Halo mass function from the simulation (circles) and the analytical fit from Warren et al. (2006). The error bars depict Poisson noise.

our small-scale (1 comoving Mpc^3) simulation is representative of the cosmic mean. Figure 4 shows the simulated halo mass function against the analytical mass function of Warren et al. (2006) that is calibrated against a suite of N-body simulations. In our simulated volume, there exists additional power at small scales, resulting in an overabundance of mini-haloes at $M \sim 10^6 M_\odot$ and less haloes than the mean at $M \gtrsim 10^{7.5} M_\odot$. Therefore, we correct the LFs

presented next by n_{sim}/n_{anyl}, the ratio of simulated halo number densities to the Warren et al. (2006) fit.

In order to understand the behaviour of the galaxy LF at high ($M_{UV} \gtrsim -15$) magnitudes, we calculate the (corrected) simulated LF at several redshifts $z = [7.3, 8, 9, 10, 12, 15]$, which are shown in Figure 5 in red squares. For comparison, we also plot the observed galaxy LFs and their fits from the HUDF galaxies at $z \leqslant 10$ (Bouwens et al. 2011; Oesch et al. 2013). It is clear that these dwarf galaxies do not follow the same power law found in L^* galaxies at similar redshifts, but their LF is nearly flat at $M_{UV} \gtrsim -12$. The mean values and their standard deviations are displayed in Table 2. All of the galaxies with these magnitudes exist in H_2-cooling haloes with $M_{vir} \leqslant 10^8 M_\odot$ (see Figure 3). The comoving density of these haloes only varies by a factor of a few during the redshift range 7–15 (Mo & White 2002). The combination with feedback and environment effects discussed in the previous section and weakly varying halo number density can explain this flat LF at $M_{UV} \gtrsim -12$. At a sufficiently high absolute magnitude, the galaxy LF should start to approach zero; however, our stellar mass resolution does not allow us to answer this question. In Figure 5, we have marked the M_{UV} of a single 1000 $M_\odot$ stellar cluster with various ages, showing the stellar mass resolution limit. We note that the simulation contains a few star particles below 1000 $M_\odot$ (see §2.2 for an explanation), which result in the dimmest galaxies at high-redshift.

Only at $z \leqslant 8$ in the simulation, a few galaxies with $M \lesssim -12$ are massive enough to host efficient star formation in atomic cooling haloes, and their number densities are consistent with the

$z = 7$ and $z = 8$ HUDF LFs. As seen in Figure 3, all galaxies with $M_{\rm UV} \leqslant -12$ are in the $M_{\rm vir} = 10^{8.5}M_\odot$ mass bin, and the galaxies dimmer than this threshold are hosted by less massive haloes. This kink in the LF signifies the transition from H_2-cooling to atomic cooling. The intersection between the LFs from the HUDF galaxies and our simulated galaxies is highly dependent on the slope α. In the $z = 9$ and $z = 10$ observed LF, the value for α is fixed to -1.73 (Oesch et al. 2013), whereas at $z = 7$ and $z = 8$, there exists enough sub-L^* galaxies to fit $\alpha = -2.01 \pm 0.21$ and -1.91 ± 0.32, respectively. Because we have found the LF to be flat and time-independent at $M_{\rm UV} \gtrsim -12$, the transition to a flat LF should only dependent on the normalization ϕ^* and slope α of more luminous galaxies.

3.3 Escape fraction

The progression of cosmic reionization from stellar sources is inherently dependent on the ionizing photon luminosity, which primarily originate from massive stars, and how much of this radiation escapes into the IGM. The production rate of ionizing photons $\dot{n}_{{\rm halo},\gamma}$ that escape from a particular halo can be parameterised into a product of four efficiency factors,

$$\dot{n}_{{\rm halo},\gamma} = f_{\rm esc} f_\gamma f_{\rm gas} f_\star M_{\rm vir}. \tag{3}$$

Here the total stellar mass $M_\star = f_{\rm gas} f_\star M_{\rm vir}$, and f_γ is the number of ionizing photons produced per stellar baryon, which can range from 6000 for a Salpeter IMF with solar metallicity to 13,000 for a metal-poor ([Z/H] $=-3.3$) population (Schaerer 2003). Then a fraction $f_{\rm esc}$ of the emitted photons escape into the IGM. This quantity is the most uncertain of the four factors that enter into reionization calculations and has been the focus of several observational and numerical campaigns.

3.3.1 Method

Radiative and supernova feedback can create channels of diffuse ionised gas from the galaxy centre to the IGM, where photons can escape from the halo relatively unobscured. Because our simulation includes both of these effects, we can calculate the UV escape fraction in post-processing without any loss in accuracy. However, we do lose any variations that might occur between data outputs.

We define $f_{\rm esc}$ as the fraction of stellar photons that exit a sphere with radius $r_{\rm vir}$ located at the halo center of mass. The UV escape fraction is directly related to the H I column density $N_{\rm HI}$ between each star and this sphere. We first divide the spherical surface into 768 HEALPix (level 3) equal-area pixels. Then for each star particle, we compute $N_{\rm HI}$ between the particle and the i-th pixel, which is converted into an transmittance $\mathcal{T}_i$ in that particular line of sight,

$$\mathcal{T}_i = \exp(-\sigma_{\rm HI} N_{{\rm HI},i}), \tag{4}$$

where we take the H I cross-section $\sigma_{\rm HI} = 1.78 \times 10^{-18}\,{\rm cm}^2$ at 21.6 eV, which is the same energy as the radiation considered in the simulation (Verner et al. 1996). Because the sphere is divided into equal-area pixels, the escape fraction for a single star particle is the average transmittance $\overline{T}$ over all of the pixels, and $f_{\rm esc}$ for the entire halo is the luminosity-weighted average of $\overline{T}$,

$$f_{\rm esc} = \sum_n^{\rm stars} L_{{\rm ion},n} \overline{T}_n \Big/ \sum_n^{\rm stars} L_{{\rm ion},n}, \tag{5}$$

where $L_{{\rm ion},n}$ is the ionizing luminosity in the halo.
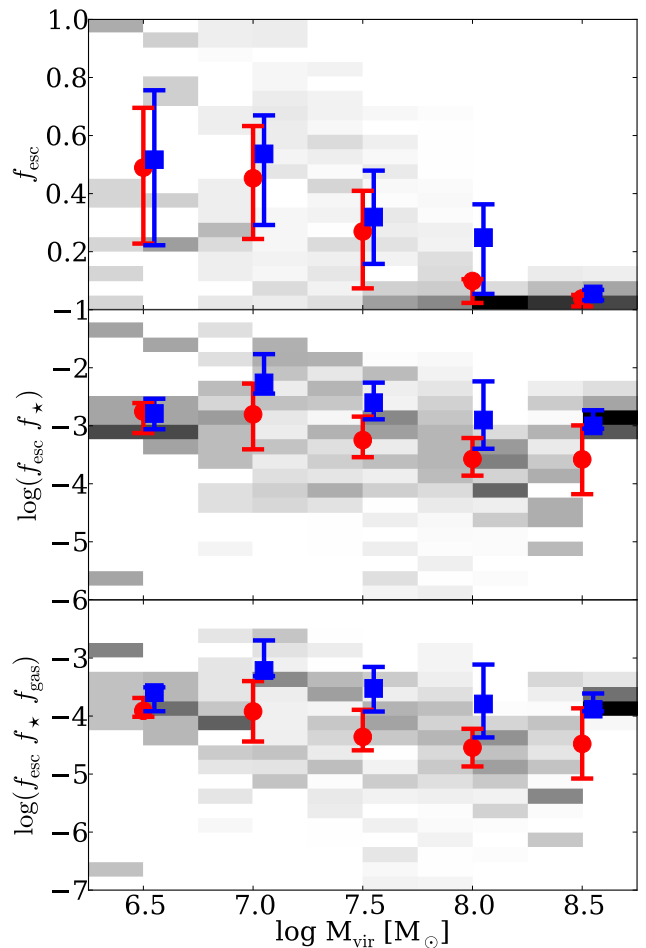

Figure 6. Probability density functions (shaded regions) for the UV escape fraction $f_{\rm esc}$ (top panel), product of the star formation efficiency $f_\star = M_\star/M_{\rm gas}$ and escape fraction (middle panel), and product of the star formation efficiency and the gas mass fraction (bottom panel) as a function of halo mass. The data are shown from all times, and the pixels are weighted by the time between snapshots. The averages and luminosity-weighted averages in 0.5 dex bins are represented by red circles and blue squares, respectively. The blue squares have been offset to the right for clarity.

3.3.2 Global trends

Our main results for the escape fraction are shown in Figure 6. We analyze the data similar to our approach with the average halo properties, where we calculate the probability distribution function for all *actively star-forming* haloes at all times. Here we only include galaxies with young (< 20 Myr) stars because massive OB stars emit almost all of the ionizing photons. In addition, we use this same age criterion to determine which star particles emit ionizing radiation in the simulation. The red circles in this Figure represent the mean quantity in 0.5 dex bins of $M_{\rm vir}$, and the blue squares denote the luminosity-weighted average of the quantities. These averages and their 1-σ deviations are listed in Table 3.

The top panel of Figure 6 shows the behaviour of $f_{\rm esc}$ with respect to halo mass. The lowest mass haloes with masses $10^{6.25} - 10^{7.25}M_\odot$ have $f_{\rm esc}$ around 50 per cent for both the mean and luminosity-weighted averages. This fraction then decreases with increasing halo mass. In the $10^{7.5}M_\odot$ bin, $f_{\rm esc}$ is 30 per cent, shrinking to a mean and luminosity-averaged value of 10 and 25 per cent, respectively, for $10^8 M_\odot$ haloes. The large scatter in the

Table 3. UV escape fraction

log $M_{\rm vir}$	Mean			Luminosity-weighted mean		
	$f_{\rm esc}$	$\log f_{\rm esc} f_\star$	$\log f_{\rm esc} f_\star f_{\rm gas}$	$f_{\rm esc}$	$\log f_{\rm esc} f_\star$	$\log f_{\rm esc} f_\star f_{\rm gas}$
(1)	(2)	(3)	(4)	(5)	(6)	(7)
6.5	$0.49^{+0.21}_{-0.26}$	$-2.75^{+0.15}_{-0.37}$	$-3.91^{+0.22}_{-0.10}$	$0.52^{+0.24}_{-0.29}$	$-2.44^{+0.25}_{-0.27}$	$-3.60^{+0.09}_{-0.32}$
7.0	$0.45^{+0.18}_{-0.21}$	$-2.80^{+0.53}_{-0.60}$	$-3.92^{+0.52}_{-0.52}$	$0.54^{+0.13}_{-0.24}$	$-2.26^{+0.50}_{-0.18}$	$-3.21^{+0.52}_{-0.10}$
7.5	$0.27^{+0.14}_{-0.20}$	$-3.25^{+0.40}_{-0.29}$	$-4.36^{+0.46}_{-0.23}$	$0.32^{+0.16}_{-0.16}$	$-2.60^{+0.35}_{-0.29}$	$-3.52^{+0.37}_{-0.40}$
8.0	$0.10^{+0.01}_{-0.08}$	$-3.57^{+0.36}_{-0.29}$	$-4.54^{+0.32}_{-0.32}$	$0.25^{+0.11}_{-0.19}$	$-2.90^{+0.67}_{-0.50}$	$-3.79^{+0.68}_{-0.58}$
8.5	$0.04^{+0.01}_{-0.03}$	$-3.58^{+0.59}_{-0.60}$	$-4.48^{+0.61}_{-0.60}$	$0.05^{+0.01}_{-0.02}$	$-3.00^{+0.27}_{-0.05}$	$-3.88^{+0.27}_{-0.04}$

Notes: Statistics are shown for galaxies at all times in 0.5 dex bins in $M_{\rm vir}$. Column (1): Virial mass in units of $M_\odot$. Column (2): Fraction of hydrogen ionizing radiation that escapes the virial radius. Column (3): Product of the UV escape fraction and star foramtion efficiency. Column (4): Product of column (3) and the gas mass fraction. Columns (5)-(7): Same as Columns (2)-(4) but ionizing luminosity weighted means are shown. Errors shown are 1-σ deviations.
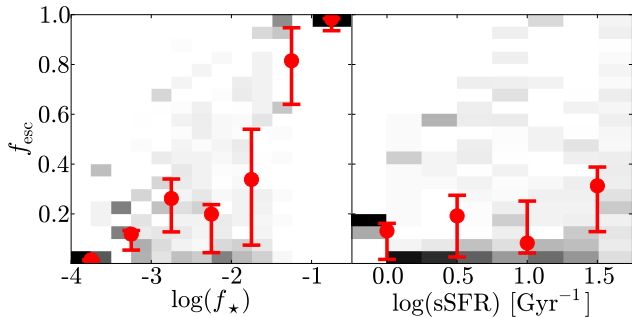
Figure 7. Same as Figure 6 but showing the UV escape fraction as a function of star formation efficiency $f_\star$ and specific SFR.

H_2-cooling haloes is created by a wide spread in the gas fraction $f_{\rm gas}$ and star formation efficiency $f_\star$ (Figure 3), where radiation in a gas-poor halo propagates through a smaller neutral column, resulting in a higher escape fraction, and vice-versa. Only four per cent of the ionizing radiation escape from the largest haloes ($M_{\rm vir} \geqslant 10^{8.25} M_\odot$) in the simulation.

The middle and bottom panels of Figure 6 show the behaviour of the products $f_{\rm esc} f_\star$ and $f_{\rm esc} f_\star f_{\rm gas}$. These products are essential ingredients in semi-analytic, and semi-numerical reionization calculations and numerical simulations that do not resolve the multiphase ISM of such small galaxies. In Section 3.1, we showed that even the H_2-cooling haloes can form stars at an appreciable rate with average values of $f_\star$ just under 0.01 for typical star-forming minihaloes. The decrease in $f_{\rm esc}$ dominates the downward trend in these products with respect to halo mass. The product $\log f_{\rm esc} f_\star$ decreases from -2.8 to -3.6 (-2.3 to -3.0) in the halo mass range $10^{6.75} - 10^{8.75} M_\odot$ for the mean (luminosity-averaged) values. Similarly, the product $\log f_{\rm esc} f_\star f_{\rm gas}$ decreases from -3.9 to -4.5 (-3.2 to -3.9) for the mean (luminosity-averaged) values in the same mass range. This illustrates that the H_2-cooling haloes may contribute significantly to the ionizing photon budget at early times ($z \gtrsim 10 - 15$) before they cease to form stars because of either Lyman-Werner or Jeans suppression.

The luminosity-weighted average is always higher than the mean value. This occurs because, at a fixed halo mass, galaxies with higher luminosities will ionise their ISM and create ionised channels out to the IGM more efficiently, boosting $f_{\rm esc}$ in such galaxies. To explore any correlation between the escape fraction and star formation, we plot the probability distribution function of $f_{\rm esc}$ as a function of the star formation efficiency $f_\star$ and the spe-

Table 4. UV escape fractions as a function of star formation efficiency and specific star formation rate

$\log f_\star$	$f_{\rm esc}$
–3.75	$0.02^{+0.00}_{-0.00}$
–3.25	$0.12^{+0.01}_{-0.06}$
–2.75	$0.26^{+0.08}_{-0.13}$
–2.25	$0.20^{+0.04}_{-0.15}$
–1.75	$0.34^{+0.20}_{-0.26}$
–1.25	$0.81^{+0.13}_{-0.18}$
–0.75	$0.99^{+0.00}_{-0.00}$
sSFR [Gyr^{-1}]	$f_{\rm esc}$
0.0	$0.13^{+0.03}_{-0.11}$
0.5	$0.19^{+0.08}_{-0.16}$
1.0	$0.08^{+0.17}_{-0.04}$
1.5	$0.31^{+0.08}_{-0.18}$

Note: The mean values are shown for galaxies at all times in 0.5 dex bins.

cific SFR (sSFR = SFR / $M_\star$) in Figure 7. The mean $f_{\rm esc}$ as a function of these quantities are also listed in Table 4. The escape fraction has a general upward trend below $f_\star = 10^{-2}$, increasing from two per cent in the most inefficient star forming galaxies to ~ 20 per cent. In galaxies with higher values of $f_\star$, the escape fraction rapidly increases to nearly unity in galaxies with $f_\star \geqslant 0.1$. This makes physical sense because if a large fraction of gas forms stars, then there will be more ionizing photons per baryon in the halo, accelerating the ionisation of the ISM and thus the escape of any ionizing radiation. Inspecting Figure 3, only the lowest-mass galaxies exhibit such high efficiencies. The scatter in this relation is caused by the variations in the halo's star formation history and environment. Looking at the behaviour of $f_{\rm esc}$ with sSFR, there is no apparent trend, and most of the galaxies $f_{\rm esc}$ values lie between 2–40 per cent.

3.3.3 *Time-dependent behaviour and correlation with star formation rates*

So far, we have focused on the star-forming properties and UV escape fractions independent of time. However, galaxies are very dynamic with widespread turbulence, H II regions growing and then recombining, and supernovae blastwaves propagating through the
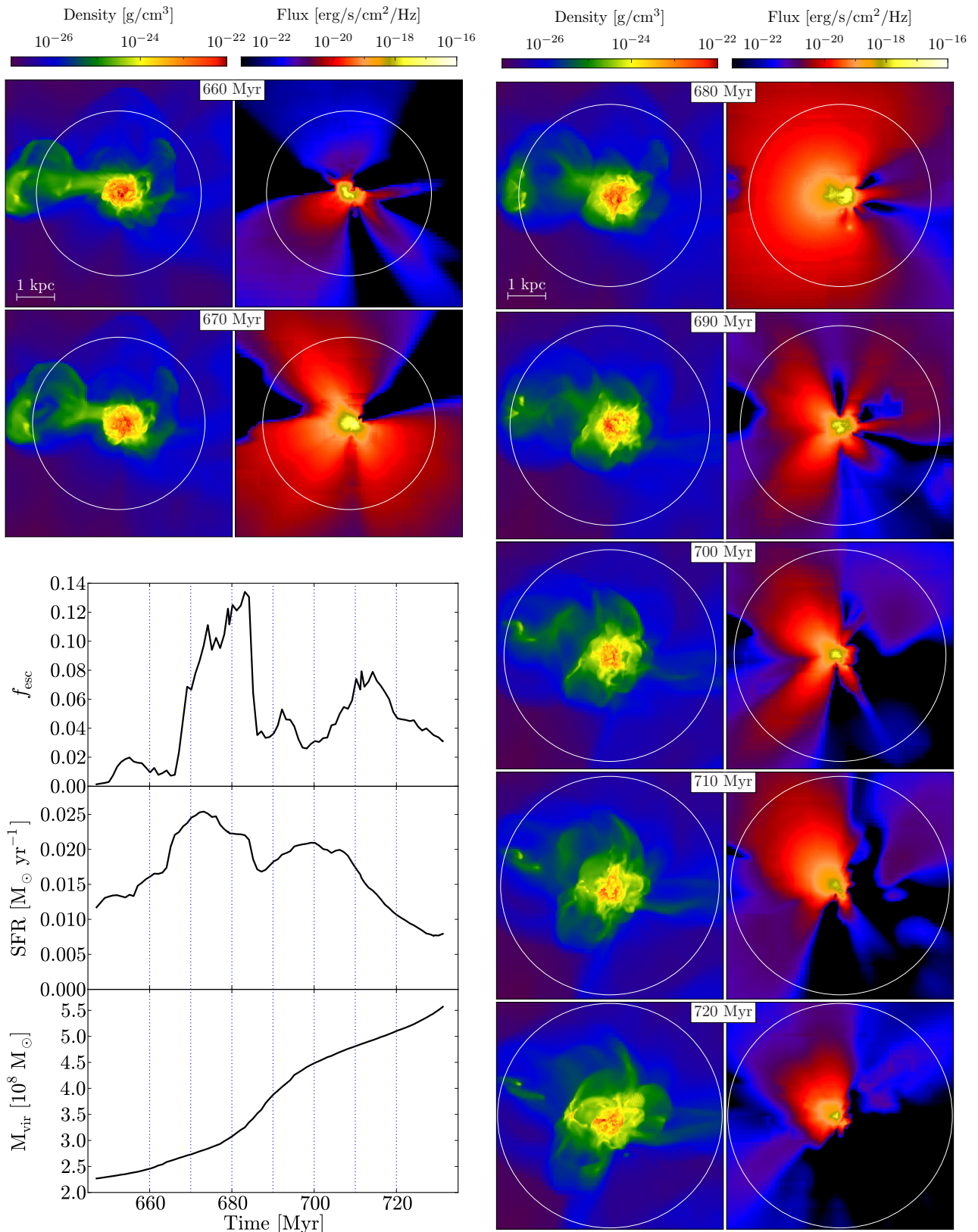
Figure 8. *Lower left:* The evolution of the UV escape fraction (top panel), SFR (middle panel), and halo mass (bottom panel) of the most massive halo, starting at $z = 8$. *Remaining panels:* Projections of density-weighted gas density (left column) and average UV ($E = 21.6$ eV) flux (right column) of the most massive halo every 10 Myr, starting at 660 Myr, which are marked in the time-evolution plot. These projections shows the variance of the gaseous structure in the galaxy and the directions in which UV radiation can escape from the halo. The projections have a field of view of 6 proper kpc and a depth of 600 proper pc. The circles show the virial radius at each time.

ISM all occurring while the halo hierarchically grows. To explore the time-dependence of the escape fraction, we focus on the most massive halo that grows from $2.2 \times 10^8 M_\odot$ to $5.5 \times 10^8 M_\odot$ during the last 80 Myr of the simulation. The lower-left panel in Figure 8 shows the escape fraction, SFR, and halo mass as a function of time, starting at $z = 8$. The remaining panels in Figure 8 show projections of density-weighted gas density and average UV flux at $E = 21.6$ eV inside of this halo.

This galaxy can sustain star formation at all times, and it experiences two epochs of stronger star formation. At $z = 8$, the SFR is $1.1 \times 10^{-2} \, M_\odot \, yr^{-1}$, which then increases to $2.5 \times 10^{-2} \, M_\odot \, yr^{-1}$ 20 Myr later and then decays as the cold dense gas is disrupted inside the galaxy. Afterward the gas can cool again and re-collapses to produce a slightly weaker burst of star formation at $2.0 \times 10^{-2} \, M_\odot \, yr^{-1}$, and it subsequently steadily decreases to $0.8 \times 10^{-2} \, M_\odot \, yr^{-1}$ at the end of the simulation.

These two bursts of star formation induce a spike in f_{esc}, which is clearly seen in Figure 8. Before the first burst, the escape fraction varies around 0.01, and then once the burst occurs, it rapidly increases to 0.13 as the H II region partially breaks out of the halo. The flux images illustrate the anisotropic escape of ionizing radiation. The peak in f_{esc} occurs 10 Myr after the peak in SFR because of the time necessary for the ionization front to propagate to the virial radius. The density projections show the irregular morphology of the ISM and an adjacent filament that is providing smooth cosmological accretion. This filament is eroded through photo-evaporation from the radiation originating in the galaxy.

At $t = 680$ Myr, a $10^8 M_\odot$ halo enters the virial radius of the most massive halo but enters in a direction that is nearly perpendicular to the projection. The additional gas sparks another burst of star formation at $t = 700$ Myr, but also increases the total H I column density between the galaxy and virial radius. This additional column and the smaller SFR causes f_{esc} to only reach 8 per cent at its peak, which then decays to 4 per cent as the SFR decreases.

The image series in Figure 8 illustrates how the direction and escape fraction of the radiation can change on timescales shorter than 10 Myr, arising from the ever-changing thermal, ionization, and density states of the ISM. For instance, the filament to the left of the halo is photo-evaporated from 660 Myr to 680 Myr, and afterwards ionizing radiation can escape in that solid angle. These directional and time-dependent properties illustrate how observations of UV flux blueward of the Lyman break are difficult to capture even if the UV escape fraction is higher than 10 per cent. However, they are unimportant global semi-analytic and semi-numerical models of reionization when the time-averaged quantities of f_{esc} are adequate.

3.4 Clumping factor

Once ionizing radiation escapes into the IGM, it can create an H II region. To remain ionised, the ionization rate must be greater than the recombination rate. Recombination in a clumpy IGM is accelerated in overdense regions because its rate is proportional to the product of the electron and proton number densities, $n_e n_p$. This enhancement factor is generally characterised by the clumping factor C that is traditionally defined as $C \equiv \langle \rho^2 \rangle / \langle \rho \rangle^2$. Finlator et al. (2012, hereafter F12) explored the variance of C with its definition, whether it is calculated as

(i) the clumping of all baryons above some threshold density to delineate between collapsed objects and the IGM,
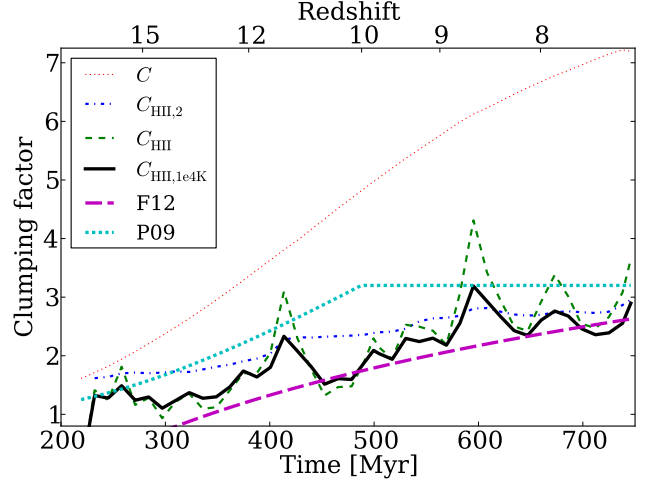
(ii) the clumping of electrons and protons,

Figure 9. Evolution of the clumping factor $C \equiv \langle \rho^2 \rangle / \langle \rho \rangle^2$ as a function of time, according to several different definitions. C shows the unfiltered clumping factor; $C_{HII,2}$ restricts the analysis to diffuse ($\rho/\rho_c < 20$) and ionised ($x > 0.1$) regions; C_{HII} (Equation 6) is weighted by x; $C_{HII,10^4 K}$ (Equation 8) is an observational temperature-corrected clumping factor of ionised gas. The peaks in the latter two definitions are caused by inhomogeneous IGM being incorporated into an H II region and subsequently photo-evaporated. The purple long-dashed line denoted by F12 is the fit from Finlator et al. (2012).

$$C_{HII} \equiv \langle n_e n_{HII} \rangle / \langle n_e \rangle \langle n_{HII} \rangle, \tag{6}$$

that can computed in only ionised regions or be weighted by the ionised volume fraction x,

(iii) a clumping factor that improves method (ii) by using the recombination rate (RR) $\alpha_B(T)$ at the temperature of the simulated gas (Shull et al. 2012),

$$C_{HII,RR} \equiv \frac{\langle n_e n_{HII} \alpha_B(T) \rangle}{\langle n_e \rangle \langle n_{HII} \rangle \langle \alpha_B(T) \rangle} \tag{7}$$

(iv) an "observational temperature-corrected" clumping factor of ionised gas that modifies method (iii) by replacing the recombination rate in the denominator with the value at $T = 10^4$ K because the observed mean IGM temperature is poorly constrained in ionised regions,

$$C_{HII,10^4 K} \equiv \frac{\langle n_e n_{HII} \alpha_B(T) \rangle}{\langle n_e \rangle \langle n_{HII} \rangle \alpha_B(10^4 K)} \tag{8}$$

F12 find that the clumping factor is sensitive to its definition, varying in the range 2–4 at $z = 6$. We find similar variations, and we show them in Figure 9, which depicts the evolution of C, two definitions of C_{HII}, $C_{HII,10^4 K}$, and the fit from F12,

$$x_{HII,v} C_{HII,10^4 K} = 9.25 - 7.1 \log_{10}(1 + z) \tag{9}$$

and the C_{100}, $z \sim 10.5$ reionization case,

$$C_{HII} = \begin{cases} 1 + \exp(-0.28z + 3.59) & (z \geqslant 10) \\ 3.2 & (z < 10) \end{cases} \tag{10}$$

from Pawlik, Schaye & van Scherpenzeel (2009).

We show two definitions of C_{HII}, where C_{HII} is weighted by the ionised fraction x, and $C_{HII,2}$ is the clumping factor for partially ionised ($x > 0.1$) gas in diffuse regions ($\rho/\rho_c < 20$). All definitions of C in the ionised regions generally increase from 1.5 to 3 from redshift 15 to 7.2, agreeing with other works (Pawlik, Schaye & van Scherpenzeel 2009; McQuinn, Oh & Faucher-Giguère 2011; Shull et al. 2012; Finlator et al. 2012). The evolution of $C_{HII,2}$

shows two abrupt increases at $z \sim 11$ and 9 followed by little evolution over the next ~ 100 Myr. Both occur when a galaxy quickly ionises the surrounding several kpc during a star formation event that has a high f_{esc}, also apparent in the jumps in ionization fraction x in Figure 1. These events are more clear in C_{HII} and $C_{\mathrm{HII},10^4\mathrm{K}}$, where the sudden increases in C occur when the H II region grows and encompasses overdensities that were previously neutral. After a sound crossing time, these clumps photo-evaporate, and the clumping factor decreases. These individual features are caused by the small simulation volume, where this behaviour in many different H II regions would average out, resulting in a smoothly increasing clumping factor. Our clumping factor is consistently higher than the F12 fit by ~ 0.25 on average because we resolve smaller systems above the cosmological Jeans mass that contribute to IGM clumpiness (Emberson, Thomas & Alvarez 2013).

4   REIONISATION MODEL

Small-scale simulations have the benefit of higher resolution, but they cannot capture the formation of rare large-scale density peaks and the evolution of global reionization from a statistically complete sample of galaxies. Low-luminosity galaxies hosted in H_2-cooling haloes should contribute a significant fraction of ionizing photons at very high redshifts because of their large number densities. On the other hand, they are susceptible to negative radiative feedback because these haloes are reliant on H_2 cooling, can be photo-evaporated from external UV radiation, and their gas can be easily expelled by supernova explosions. To assess the global impact of these smallest galaxies during reionization, we utilise the mean galaxy properties and escape fractions from our simulation in a semi-analytical model of reionization.

4.1   Method

We compute the evolution of the hydrogen ionised fraction x by solving

$$\dot{x} = \frac{\dot{n}_\gamma}{\bar{n}_{\mathrm{H}}} - \frac{x}{\langle t_{\mathrm{rec}} \rangle}, \tag{11}$$

where $\dot{n}_\gamma$ is the comoving ionising photon emissivity, $\bar{n}_{\mathrm{H}}$ is the mean comoving hydrogen number density, and $\langle t_{\mathrm{rec}} \rangle = [C(z)\alpha_B n_{\mathrm{H}}(1+Y/4X)(1+z)^3]^{-1}$ is the volume-averaged hydrogen recombination time. $X = 0.76$ and $Y = 1 - X$ are the hydrogen and helium number fractions, respectively (Shapiro & Giroux 1987). We use the clumping factor C_{HII} from Pawlik, Schaye & van Scherpenzeel (Equation 10; 2009) and start with an initial ionised fraction of 10^{-5} at $z = 30$. We integrate this equation until the volume is completely ionised, giving a full reionisation history from which we can calculate the optical depth due to Thomson scattering,

$$\tau_e = \int_0^\infty dz \frac{c(1+z)^2}{H(z)} x(z) \sigma_T \bar{n}_H (1 + \eta Y/4X), \tag{12}$$

where $H(z)$ is the Hubble parameter, σ_T is the Thomson cross-section. We assume that the helium is singly ionised ($\eta = 1$) at $z > 3$ in the same volume fraction as hydrogen and doubly ionised ($\eta = 2$) at later times. Comparing the calculated τ_e of our models to the observed values from WMAP and *Planck*, $\tau_e = 0.089^{+0.012}_{-0.014}$, can place constraints on the timing of reionisation and the ionising emissivity.

4.1.1   Ionizing emissivity

Most of the uncertainties are hidden in the ionising photon emissivity (see Equation 3). For a halo mass independent model, $\dot{n}_\gamma = f_{\mathrm{esc}} f_\gamma \dot{\rho}_\star$, where $\dot{\rho}_\star$ is the SFR density, and f_γ is the photon to stellar baryon number ratio. However, we have shown that the escape fraction and SFRs are a strong function of halo mass M; therefore, we consider

$$\dot{n}_\gamma = \int_{M_{\mathrm{min}}}^\infty f_{\mathrm{esc}} f_\gamma (f_{\mathrm{gas}} f_\star \dot{f}_c M_{\mathrm{vir}}) \, dM_{\mathrm{vir}}, \tag{13}$$

where *all* of the factors inside the integral are functions of halo mass, and the product inside the parentheses is the cosmic SFR density in halo masses between M and $M + dM$. We take $M_{\mathrm{min}} = 10^{6.5} M_\odot$ from our simulation. Here $\dot{f}_c$ is the time-derivative of the collapsed fraction that is calculated with the ellipsoidal variant of Press-Schetcher formalism (Press & Schechter 1974; Sheth, Mo & Tormen 2001) with the same cosmological parameters used in the simulation.

We compute $\dot{n}_\gamma$ by discretising the integral in Equation (13) into mass bins of $\log \Delta(M_{\mathrm{vir}}/M_\odot) = 0.5$ in $\log(M_{\mathrm{vir}}/M_\odot) \in [6.25, 12.75]$. At $\log(M_{\mathrm{vir}}/M_\odot) < 8.75$, we utilise the luminosity weighted mean values of $f_{\mathrm{gas}} f_\star f_{\mathrm{esc}}$ from the simulation (Table 3). For more massive haloes that are not sampled by our simulation, we assume a mass-independent values (cf. Alvarez, Finlator & Trenti 2012), $(f_\star, f_{\mathrm{esc}}, f_{\mathrm{gas}}) = (0.03, 0.05, \Omega_b/\Omega_m)$.

Metal-poor stars can produce up to a factor of two more ionising photons per stellar baryon, compared to their solar metallicity counterparts, because of higher surface temperatures. To account for this effect, we utilise the photon to stellar baryon ratio $f_\gamma(Z)$ from Schaerer (2003, their Equation 1). Then we can express $f_\gamma = f_\gamma[Z(M_{\mathrm{vir}})]$ through two relations: (i) the local dwarf galaxy metallicity-luminosity relation (Woo, Courteau & Dekel 2008),

$$\log(Z) = -3.7 + 0.4 \log\left(\frac{M_\star}{10^6 M_\odot}\right), \tag{14}$$

and (ii) our simulated $M_\star - M_{\mathrm{vir}}$ mean values (Table 1), resulting in an decreasing γ with increasing M_{vir}.

Lastly, we include emissivity from Population III stars in one model. They only form in metal-free haloes that are susceptible to LW feedback and metal enrichment. Simulations that include these physics show the SFR increasing for the first ~ 100 Myr, and afterwards the SFR becomes approximately constant prior to reionization (e.g. Wise et al. 2012b; Xu, Wise & Norman 2013). Therefore, we assume a constant Pop III SFR of 5×10^{-5} $M_\odot$ yr^{-1} Mpc^{-3}, starting at $z = 30$, with $f_\gamma = 60,000$ (Schaerer 2002). This corresponds to $\dot{n}_\gamma = 1.1 \times 10^{50}$ s^{-1} cMpc^{-3}. Note that this emissivity does not enter the integral in Equation (13) but adds a constant term to $\dot{n}_\gamma$.

4.1.2   Dwarf galaxy suppression

The suppression of star formation occurs in low-mass haloes that are susceptible to negative feedback through photo-dissociation, gas blowout, and/or photo-evaporation. Our simulation showed the halo-galaxy occupation fraction f_{host} decreasing from an initial value f_0 to a final value f_1 after a sound crossing time

$$t_{\mathrm{sc}} \approx 200 \text{ Myr} \left(\frac{M}{10^8 M_\odot}\right)^{1/3} \left(\frac{1+z}{10}\right)^{-1} \left(\frac{\Omega_{\mathrm{m}} h^2}{0.15}\right)^{-1/3}. \tag{15}$$

We apply this suppression when the filtering mass $M_{\mathrm{F}}(t_{\mathrm{F}}) > M_{\mathrm{vir}}$ by multiplying $\dot{n}_\gamma$ by

$$f_{\text{host}}(M, t) = A - B \tanh\left(\frac{t - t_{\text{F}} - t_{\text{sc}}/2}{t_{\text{sc}}/3}\right), \qquad (16)$$

where $A = (f_0 + f_1)/2$ and $B = (f_0 - f_1)/2$. To calculate the filtering mass (Equation 2), we use a simple model that uses the Jeans mass M_{J} of an ionised IGM with $T = 10^4$ K and $\rho = \Omega_b \rho_c$.

Figure 2 shows that star formation is suppressed in galaxies that cannot cool through atomic transitions. Thus, we only use this transition for the mass bins centered on $\log(M_{\text{vir}}/M_\odot) = (7.0, 7.5, 8.0)$, where we use $f_0 = (0.3, 0.5, 1.0)$ and $f_1 = (0.01, 0.15, 0.5)$, respectively. For $\log(M_{\text{vir}}/M_\odot) = 6.5$, we use $f_{\text{host}} = 2.4 \times 10^{-4}$, the time-averaged value, because these extremely low-mass galaxies are sporadic and rare (see §3.1). Lastly, we do not alter the emissivities of the atomic cooling haloes with $\log(M_{\text{vir}}/M_\odot) > 8.25$.

4.2 Results

Here we consider three models that progressively add more ionising radiation sources: (i) star formation only in haloes with masses $M_{\text{vir}} > 10^{8.25} M_\odot$ that are approximately atomic cooling haloes, (ii) plus star formation in minihaloes with masses $M_{\text{vir}} > 10^{6.25} M_\odot$, and (iii) plus Pop III star formation. Figure 10 shows the main results from our semi-analytic reionization models.

The model that restricts star formation to atomic cooling haloes reionises the universe at $z = 5.5$, resulting in $\tau_e = 0.059$, which is typical of models either only considering atomic cooling haloes with low escape fractions that are similar to local dwarf galaxies or only including observable galaxies at $z \gtrsim 6$ (e.g., see the $M_{\text{UV}} = -17$ model of Robertson et al. 2013). To explain the discrepancy between the observed values of τ_e and the models that include only currently observable galaxies, high escape fractions may be invoked (e.g. Kuhlen & Faucher-Giguère 2012; Alvarez, Finlator & Trenti 2012; Robertson et al. 2013) and other sources of ionising photons, such as X-ray binaries (Power et al. 2013; Fragos et al. 2013) and Pop III stars (Ahn et al. 2012). Kuhlen & Faucher-Giguère and Robertson et al. both used a mass-independent description of the star formation efficiency and escape fraction, but Alvarez, Finlator & Trenti presented a simple model that delineated between low- and high-mass dwarf galaxies with $f_{\text{esc}} = (0.8, 0.05)$, respectively. None of these recent studies considered minihaloes because they are very susceptible to negative feedback; however, our simulation shows that they can indeed form a non-negligible amount of stars with high escape fractions.

Our model (ii) includes such low-luminosity galaxies, which boosts τ_e to 0.093 that is very close to the best-fit value from *Planck* of $\tau_e = 0.0925$ illustrated in the middle panel of Figure 10. This model reionises the universe at $z = 6.4$. The bottom panel of Figure 10 shows that the ionising photon emissivity is already 2×10^{50} s^{-1} cMpc^{-3} at $z = 20$ compared to the negligible emissivity (2×10^{48} s^{-1} cMpc^{-3}) when minihaloes are not included. It continues to rise until it reaches 8×10^{50} s^{-1} cMpc^{-3} at $z \sim 10$. Eventually these galaxies are photo-suppressed, and the total ionising emissivity converges to model (i) at $z \sim 6$ that are consistent with observational constraints (Kuhlen & Faucher-Giguère 2012; Becker & Bolton 2013). These smallest galaxies have $f_{\text{esc}} \sim 0.5$, and their host haloes collapse much earlier than the atomic cooling haloes, leading to the boost at very high redshifts. The top panel of Figure 10 shows this early time behaviour produces a more extended reionisation history with an ionised volume fraction of $x = 0.2$ by $z = 14$ and $x = 0.5$ by $z = 9.4$. The top panel of Figure 11 shows the instantaneous fractional emis-
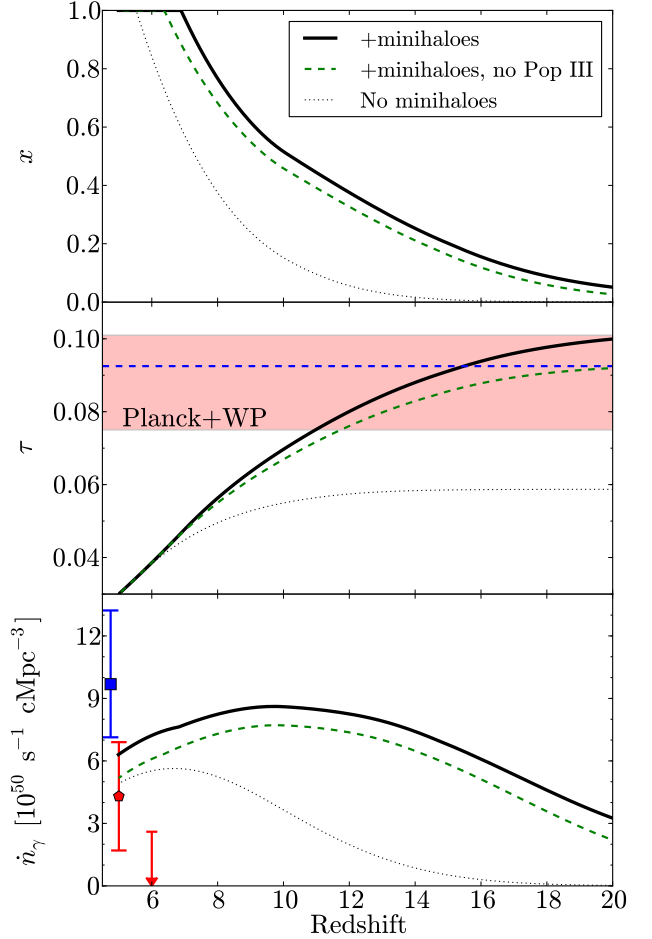
Figure 10. Ionization histories for models that include only atomic cooling haloes (dotted lines), adding Pop II star-forming minihaloes (dashed lines), and including Pop III star formation (solid lines). The luminosity-weighted mean of the escaping ionising luminosity shown in Tables 1 and 3 (solid lines), are used. *Top panel:* Evolution of ionised mass fraction. *Middle panel:* Corresponding Thomson scattering optical depth with the Planck+WMAP9 best fit and 1-σ errors shown. *Bottom panel:* Comoving ionising photon emissivity that escape into the IGM. The points denote constraints from the transmissivity through the Lyα forest from Kuhlen & Faucher-Giguère (red circle and upper limit; 2012) and Becker & Bolton (blue square; 2013). It should be noted that in the range $z = 2 - 5$, Becker & Bolton found ionising photon emissivities a factor of ~ 2 higher than Kuhlen & Faucher-Giguère.

sivity from haloes below three different mass thresholds that are often used for suppression, $T_{\text{vir}} = 10^4$ K, $V_c = 30$ km s^{-1}, and $M_{\text{vir}} = 2 \times 10^9 M_\odot$. The H$_2$-cooling haloes provide 75 per cent of the ionising emissivity at $z = 15$, dropping to 10 per cent by $z = 7$, as they are photo-suppressed, and larger galaxies are the main source of reionisation at later times. Similar trends are seen in the other two halo mass thresholds, where at $z = 10$, haloes with $V_c \leqslant 30$ km s^{-1} and $M_{\text{vir}} \leqslant 2 \times 10^9 M_\odot$ produce 50 and 80 per cent of the ionising emissivity, respectively. The bottom panel of Figure 11 shows the cumulative fraction of ionising radiation that originates from haloes below the same halo mass thresholds. The key point to take from these results at $z = 6$ is that 27, 36, and 56 per cent of the total ionising photon budget are created in haloes with $T_{\text{vir}} \leqslant 10^4$ K, $V_c \leqslant 30$ km s^{-1}, and $M_{\text{vir}} \leqslant 2 \times 10^9 M_\odot$, respectively. Thus, we conclude that *the lowest luminosity galax-*
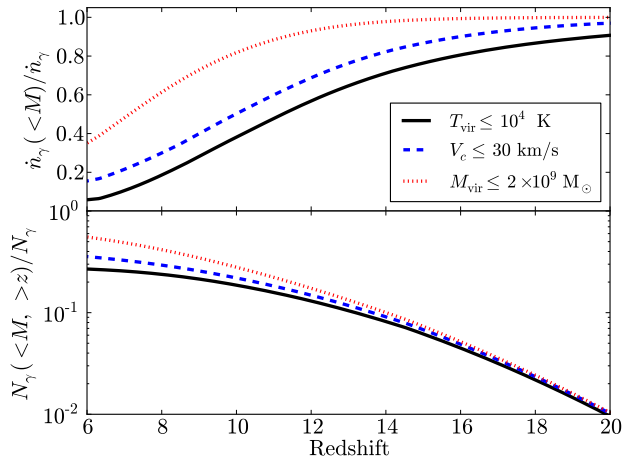
Figure 11. *Top panel:* The fractional instantaneous ionising emissivity from haloes below three mass thresholds typically used for the suppression of star formation, $T_{\rm vir} = 10^4$ K (solid black), $V_c = 30$ km s^{-1} (blue dashed), and $M_{\rm vir} = 2 \times 10^9 M_\odot$ (red dotted). Low-mass haloes dominate the photon emissivity at high redshifts, producing an ionisation fraction of 20 per cent by $z = 14$, which are photo-suppressed at lower redshifts. *Bottom panel:* The cumulative fraction of ionising photons emitted from galaxies contained in haloes below the same thresholds as the top panel. These data demonstrate that even the H$_2$-cooling haloes contribute nearly 30 per cent to the total photon budget and should not be neglected in reionisation calculations.

ies play an integral role in the reionisation of the universe but are eventually suppressed as they are engulfed by an increasing UV radiation background.

Short-lived Pop III stars provide an additional source of ionising photons, where they ionise the surrounding few kpc, and then this H II region quickly recombines. However in our model, they have a low-level contribution to the ionising photon budget, increasing the $\dot{n}_{\rm ion}$ by 1.1×10^{50} s^{-1} cMpc^{-3}. This increases τ_e to 0.106 that is in the upper 1-σ bound of the *Planck* results and results in complete reionisation at $z = 6.9$.

For mass-independent models of reionisation, it is useful to consider luminosity-weighted mean value of $f_{\rm esc}$ and the host halo mass, which are shown as a function of redshift in Figure 12. At early times, the low-luminosity galaxies are not suppressed and are the biggest sources of the ionising photon budget, which is apparent by the mean halo mass of $10^{7.2} M_\odot$ and $f_{\rm esc} = 0.46$ at redshift 20. As these galaxies are suppressed, the halo mass scale increases to $\sim 10^{10} M_\odot$ by redshift 6 while the mean escape fraction gradually drops to $f_{\rm esc} = 0.05$, which is the assumed escape fraction of these larger galaxies. This time-dependent behaviour is generally true for any model that considers multiple galaxy populations that are suppressed and unaffected by feedback mechanisms (cf. Alvarez, Finlator & Trenti 2012); however, the evolution of $f_{\rm esc}$ is much slower than the one assumed in Haardt & Madau (2012) as shown in Figure 12.

Our results are well-fit by analytic functions and can be easily utilised in reionisation models. Fitting the time-dependence of $f_{\rm esc}$ with a pure Gaussian had errors up to 20 per cent at early times and is better fit with a Voigt profile,

$$\langle f_{\rm esc} \rangle_{\rm L}(z) = 0.54 - 544\, G(z, \sigma, z_0)\, L(z, \Gamma, z_0), \qquad (17)$$

where G and L are Gaussian and Lorentzian distribution functions that are normalised to unity, respectively. Our best-fit model has
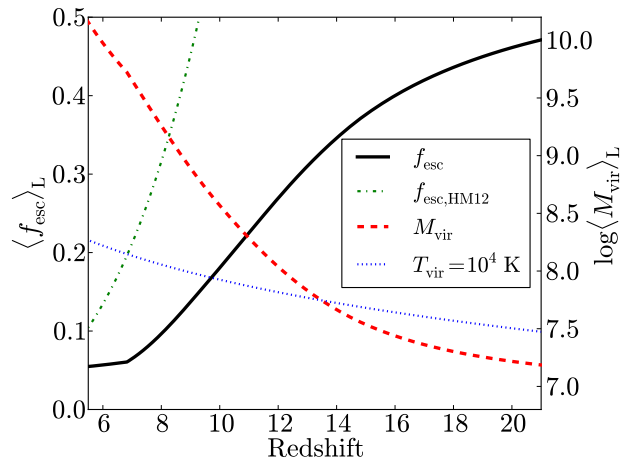

Figure 12. Ionizing luminosity weighted mean values of the ionising photon escape fraction (black solid) and halo mass (red dashed) in the model that includes minihaloes and Pop III star formation. For comparison, the escape fraction from Haardt & Madau (2012) (green dash-dotted) increases much more rapidly with redshift, and the blue dotted line shows the virial mass of a $T_{\rm vir} = 10^4$ K halo is shown, taking the mean molecular weight $\mu = 0.6$.

$\sigma = 19.6$, $\Gamma = 7.26$, and $z_0 = 5.8$ and is only valid for $z > z_0$. Prior to reionisation, the luminosity-weighted halo mass scale asymptotes to linear relations at early and late times and can be fit by a rotated hyperbola. But for computational convenience, we can fit the behavior with

$$\log \langle M_{\rm vir} \rangle_{\rm L}(z) = 7.0 + (0.25 + 2.96 \times 10^{-4} z^{3.16})^{-1}. \qquad (18)$$

Both fits are good to within 3 per cent at $z > 5.8$, where our $f_{\rm esc}(z)$ fit reaches a minimum. These fits encapsulate the effects of suppression of the lowest mass dwarf galaxies that have high escape fractions. Coupled with our mass-dependent dwarf galaxy properties presented in §3, this resulting reionisation history demonstrates the role of high-redshift, photo-suppressible dwarf galaxies during reionisation.

5 DISCUSSION

We have demonstrated that low-luminosity galaxies play a key role during the early phases of reionisation. The exact properties of a particular high-redshift dwarf galaxy most critically depend on the star formation history and the ionization and thermal properties of its local environment. For instance, the magnitude of radiative and supernova feedback in their progenitors will regulate the gas and metal content of the galaxy, thus affecting the strength of radiative cooling and star formation in the dwarf galaxy.

As previous studies have shown (e.g. Clarke & Oey 2002; Wise & Cen 2009; Fernandez & Shull 2011; Benson, Venkatesan & Shull 2013), ionising radiation mainly escapes through low-density channels that are created by ionisation fronts or supernovae. The location and strength of star formation and galaxy morphology can both influence the UV escape fraction. Thus, resolving star-forming clouds and the multi-phase ISM are necessary requirements for any simulation that aims to measure the escape fraction. Furthermore, environmental properties, in particular, the incident background radiation can affect the formation of the first galaxies and their escape fractions. First, any Lyman-Werner radiation background will suppress H$_2$ formation and thus Pop III stars in the progenitors. If Pop

III star formation is delayed to haloes with $M \gtrsim 10^7 M_\odot$, the H II region and SN blastwave may fail to breakout of the halo, possibly leading to prompt metal-enriched star formation (Whalen et al. 2008; Ritter et al. 2012). Second, any ionising radiation background will photo-evaporate the gas in low-mass haloes over a sound-crossing time. However, photo-evaporation may boost the escape fraction for a short period if the halo is already hosting active star forming regions. If the outer layers of gas are photo-evaporated by an external source, the neutral hydrogen column density between the halo center and the IGM will decrease, causing an increase in escape fraction in principle. On the other hand, this reduces the amount of gas available for future star formation in small galaxies. If the halo does not accrete additional gas from smooth accretion or a merger within a sound-crossing time, the SFR and escape fraction will steadily decrease, where we showed a similar case of a correlation between SFR and escape fraction in Figure 8.

Although the SFRs in the lowest-mass galaxies are small, their roles in reionisation are not insignificant. Now we turn our attention to the implications of our results on reionisation, their observational prospects, differences with previous work, and caveats of our study.

5.1 Implications for reionisation

The idea of the faintest galaxies providing the majority of the ionising photon budget of reionisation is not a new one. However, our work provides convincing evidence that stars form in these galaxies before becoming photo-suppressed by internal stellar feedback and external radiative feedback. Their star formation efficiencies are not significantly lower than atomic cooling haloes, but their low masses lead to low SFRs of $10^{-3} - 10^{-4}$ M$_\odot$ yr^{-1} with about half of the ionising radiation escaping into the IGM. Combined with a high number density of their host haloes, their contribution to reionisation should not be neglected, especially at very high redshift ($z \gtrsim 10$). Some of these galaxies are initially embedded in a cool and neutral ISM, most likely in a relic H II region from Pop III stars, but as global reionisation proceeds, they are likely embedded in larger H II regions, slowly being photo-evaporated over a sound crossing time. Then larger galaxies that are hosted by atomic cooling haloes provide the majority of ionising radiation, as shown in Figure 12. In a statistical sense, there will probably be no detectable transition in the reionisation or SFR history between these two source types because they form coeval. A significant fraction of galaxies that are initially photo-suppressed will likely host star formation shortly afterward because rapid mass accretion rates at high-redshift will allow for efficient cooling and star formation even in the presence of a UV radiation field.

This scenario leads to an extended period of reionisation, where the universe has an ionised mass fraction of 10 and 50 per cent by $z \sim 17$ and $z \sim 10$, respectively, eventually becoming completely reionised by $z \sim 6.5$ (see Figure 10). Such an extended ionisation history produces a Thomson scattering optical depth $\tau_e = 0.093$ and an ionising emissivity that are consistent with *Planck* and Lyα forest observations, respectively. We stress that the faintest galaxies should not be overlooked in reionisation models and provide the key to matching the latest ionisation constraints, resolving any tension between CMB observations and Lyα forest observations at $z \sim 6$.

5.2 Observational prospects

Figure 13 shows the absolute magnitude at 1500 Å of a typical dwarf galaxy that contributes to reionisation as a function of red-
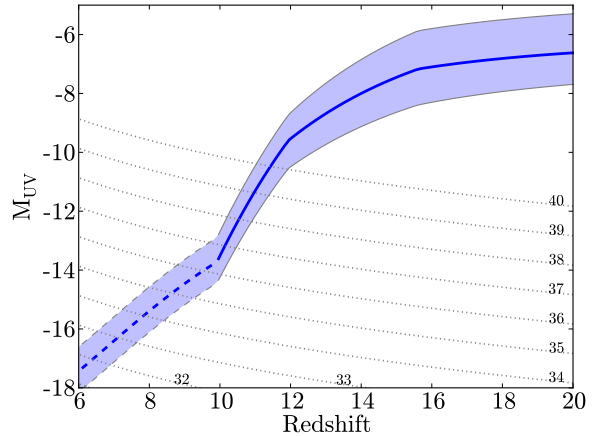
Figure 13. Absolute UV magnitude at 1500 Å for the typical dwarf galaxy contributing to reionisation. The solid line uses the mean $M_\star - M_{\rm vir}$ relation shown in Table 1 to convert the luminosity-weighted average halo mass in Figure 12, where the shaded areas show the 1-σ deviations. The dashed lines extrapolate to halo masses $M \geqslant 10^{8.5} M_\odot$. The thin dotted lines show the apparent magnitude that are denoted above the lines.

shift. Here we take the luminosity-averaged halo mass, shown in Figure 12 and show the average and 1-σ deviations of $M_{\rm UV}$ from Table 1. Even at $z < 10$, the continuum radiation from these typical galaxies is well below the detection limits in the HUDF and *Cluster Lensing And Supernova survey with Hubble* (CLASH; Postman et al. 2012) campaigns.

Recall that our calculation of $M_{\rm UV}$ only considers stellar radiation and not nebular emission. In particular, Lyα emission from the H II region will be strong in these galaxies, perhaps having an intrinsic equivalent width (EW) as high as 1500 Å (Schaerer 2002; Johnson et al. 2009; Dijkstra & Wyithe 2010). In a static ISM/IGM, Lyα photons would be absorbed by the surrounding neutral medium. However, Dijkstra & Wyithe (2010) showed that a $\gtrsim 50$ km s^{-1} H I outflow allows for 10–20 per cent of the Lyα emission to be transmitted through a neutral IGM, still resulting in a strong EW of $\sim$100 Å (see also Verhamme, Schaerer & Maselli 2006; Verhamme et al. 2008). Inspecting the most massive galaxy in our simulation at redshifts 12 and 7.3, we find that the intrinsic $\log L_{\rm Ly\alpha} = (37.3, 40.3)$ erg s^{-1} in a sphere of radius $2r_{\rm vir}$, assuming that all ionising radiation is absorbed by the nearby neutral IGM. This is comparatively lower than $\log L_{1500} = (36.0, 39.0)$ erg s^{-1} from stellar emission alone. At these respective redshifts, the galaxy has a total mass of $2.7 \times 10^7 M_\odot$ and $6.8 \times 10^8 M_\odot$ and a stellar mass of $1.5 \times 10^4 M_\odot$ and $3.5 \times 10^6 M_\odot$. Outflows are ubiquitous in high-redshift dwarf galaxies, and we thus expect that a significant fraction of Lyα emission would be transmitted through the IGM. We intend to follow-up the observable Lyα line profiles and strengths in a more complete statistical sample of high-redshift galaxies presented in Xu, Wise & Norman (2013).

Even with the exquisite sensitivity of JWST, the typical reionising sources will not be detectable. Only galaxies with a SFR > 0.1M$_\odot$ yr^{-1} will be detected in 10^6 s exposures (Pawlik, Milosavljević & Bromm 2013). However, surveys of gravitational lensed regions may uncover a significant fraction of such galaxies, for instance, median magnifications are between 2–15 in the CLASH fields (Bouwens et al. 2012a; Bradley et al. 2013). Searches with narrow-band filters at a particular redshift around the Lyα λ1215,

He II λ1640, and Hα λ6536 lines (e.g. Johnson et al. 2009; Paardekooper, Khochfar & Dalla Vecchia 2013) in gravitational lensed fields may be the best strategy for detecting high-redshift dwarf galaxies (e.g. Zackrisson et al. 2012). If detected, these faint galaxies would be highly unobscured because the majority of the radiation would be propagating through ionised channels in the ISM and surrounding IGM. Would they constitute *a new galaxy class* that only exist prior to cosmic reionisation, existing in large-scale neutral regions of the universe embedded in their own H II region? Because of their unique environment, they would have no direct present-day analogue, and models that include radiative Population III and II/I stellar feedback, creating local H II regions and outflows are necessary to make solid predictions of the connection between their intrinsic and observable properties.

5.3   Comparison to previous work

5.3.1   Star formation rate and efficiency

W12 found that the mean stellar metallicity and its distribution function were good discriminates of a plausible star formation and feedback implementation, avoiding the typical galaxy formation simulation "overcooling problem". Little is published on simulated stellar metallicity data in the first galaxies (however, see Ricotti & Gnedin 2005), so we will compare the SFRs and efficiencies to previous work.

Ricotti, Gnedin & Shull (2008) found a power law dependency between halo mass and star formation efficiency with a slope of 1.5 and 2 in their weak and strong feedback cases in their cosmological radiation hydrodynamics simulations of early galaxy formation. In their weak case, $\log f_\star \simeq -3.0$ and -1.5 at halo masses of $10^7 M_\odot$ and $10^8 M_\odot$, respectively. We see no such trend in $f_\star$ (see Figure 3), where we find a decreasing trend at $M \lesssim 10^{7.5} M_\odot$ with a large scatter because the outflows from the initial star formation event temporarily suppresses any further star formation. At larger masses it slowly increases to 1–3 per cent at $M = 10^{8.5} M_\odot$, where we would expect it to plateau at higher halo masses. It is wise to disregard their power law fit at higher masses because it diverges, and the star formation efficiency probably levels out at higher masses (see Pawlik, Milosavljević & Bromm 2013).

We find acceptable agreement with the H$_2$-cooling haloes in the "LW+RT" simulation of Pawlik, Milosavljević & Bromm (2013) that considered most of the physics included in our simulation with the exception of a model of Population III star formation and feedback, metal cooling, and radiation pressure. However, they include the effects of stellar radiative feedback in their work, which plays a significant role in regulating star formation in these low-mass galaxies. They find $\log f_\star \simeq -3.0$, slightly lower than our results, which could come from the lack of metal-line cooling, resulting in lower cooling rates and thus star formation efficiencies. On the other hand, there are similarities between our results, in that, they have a similar scatter and no dependence on halo mass. Their values of $f_\star$ increase rapidly to ~ 0.1 when it can atomically cool, which is about a factor of five higher than our results. Lastly, they find similar gas fractions $f_{\rm gas} \gtrsim 0.1$ that are depressed in H$_2$-cooling haloes.

Biffi & Maio (2013) analyzed a cosmological simulation that samples mostly H$_2$-cooling haloes (up to $7 \times 10^7 M_\odot$ at $z = 9$) and includes distinct models of Pop III and Pop II/I star formation. In their $z = 9$ data, they find a suppressed gas fraction of 2–5 per cent in haloes with $M \sim 10^6 M_\odot$, rising to 10 per cent in $\sim 10^7 M_\odot$ haloes. We find a similar suppression, but the haloes only recover

to $f_{\rm gas} = 0.1$ in $10^8 M_\odot$ haloes. We suspect that their elevated gas fractions result from the lack of radiative feedback. Star formation is suppressed below a halo mass scale of $5 \times 10^6 M_\odot$, agreeing with our results. In haloes with $M \geqslant 10^7 M_\odot$, they find stellar mass fractions ($M_\star/M_{\rm vir}$) between 10^{-3} and 10^{-4}. The stellar mass fractions in our work in these haloes are in the range $1 - 4 \times 10^{-4}$. Their objects with high star formation efficiencies most probably arises from the higher gas fractions. Lastly, they find haloes with a very small $f_\star = 10^{-6} - 3 \times 10^{-5}$, which is below our stellar mass resolution of 1000 $M_\odot$.

5.3.2   UV Escape fraction

In the past five years, theoretical work has favored high escape fractions between $0.1 - 0.8$ from galaxies with total masses $M \lesssim 10^9 M_\odot$ (Wise & Cen 2009; Razoumov & Sommer-Larsen 2010; Yajima, Choi & Nagamine 2011; Paardekooper, Khochfar & Dalla Vecchia 2013). We also find high average $f_{\rm esc}$ values of $\sim$0.5 but only in haloes with $M \lesssim 2 \times 10^7 M_\odot$, which are then photo-suppressed. The UV escape fraction steadily decreases with increasing halo mass to a luminosity-weighted average of 25 and 5 per cent for $10^8 M_\odot$ and $10^{8.5} M_\odot$ haloes, respectively.

Why do we find lower escape fraction in low-mass atomic cooling haloes than other recent studies? To explain this, we can describe the shortcomings of Wise & Cen (2009), who extracted haloes from cosmological simulations without radiative cooling, star formation, and feedback as initial conditions. These haloes had a gas fraction near the cosmic mean, which then proceeded to monolithically collapse in the re-simulations because they were only allowed to radiatively cool. This produced unrealistically strong starbursts in their ten halo sample with a star formation efficiencies of 5–10 per cent and $f_{\rm esc} \sim 0.4$ for haloes with $M \gtrsim 10^8 M_\odot$. For such strong starbursts, we found that $f_{\rm esc} \gtrsim 0.5$ (see Figure 7 and Table 4). Because the $M = 10^8 - 10^9 M_\odot$ haloes in Razoumov & Sommer-Larsen (2010) and Yajima, Choi & Nagamine (2011) were the smallest in their sample, they would have suffered the same aberration, which is a general consequence of missing early phases of galaxy formation, leading to the over-cooling problem. If the haloes were allowed to form stars throughout their assembly, then the SFRs and efficiencies would have been regulated over this period, leading to more controlled star formation events and lower $f_{\rm esc}$ values. Analogous behavior for the escape fraction was seen in the metal cooling only simulation of W12, where the most massive halo underwent a catastrophic cooling event once it reached $T_{\rm vir} \sim 10^4$ K, resulting in a SFR an order of magnitude higher than the RP simulation, which is presented here, that proceeded to reionise nearly the entire simulation volume.

Our results for $M \sim 10^7 M_\odot$ haloes are similar to the results of Paardekooper, Khochfar & Dalla Vecchia (2013) before their uniform UV background activates at $z = 12$. Then their average $f_{\rm esc}$ values increase from $\sim$0.6 to nearly unity at $z = 6$. Similar evolution occurs in $10^8 M_\odot$ haloes, increasing from $\sim$0.4 to 0.95. We suspect that variations in our analyses, where they consider all star clusters and whereas we only consider young (< 20 Myr) star clusters, have caused the discrepancy between our two efforts. As the haloes are photo-evaporated by the UV background at later times in their simulation, the UV stellar radiation from the older stars can escape more easily through a lower neutral column density, causing higher $f_{\rm esc}$ values at later times. They also see a similar but more abrupt transition from H$_2$-cooling to atomic cool-

ing haloes as the primary source of ionising photons as the former objects are photo-suppressed.

5.3.3 *Reionisation history*

The inclusion of galaxies that are liable to photo-suppression into a reionisation model produces an extended reionisation history with the ionised fraction increasing from $x = 0.2$ at $z = 14$ to $x = 0.5$ at $z = 9$, and finally becoming completely reionised by $z \simeq 6.5$. This history is a consequence of a halo mass dependent escape fraction and SFRs, extending down to $10^{6.5} M_\odot$ haloes that are gradually photo-suppressed. It is very similar to the one presented in (Haardt & Madau 2012), but the evolution of $f_{\rm esc}$ and the cosmic SFRs are much different in nature. Because galaxies can form in H_2-cooling haloes, non-negligible SFRs extend to $z \sim 15 - 30$, reducing the need for an escape fraction of unity at $z > 12.5$ in their model. Recently a few groups (Shull et al. 2012; Kuhlen & Faucher-Giguère 2012; Robertson et al. 2013) calculated a reionisation history that was based on the latest HUDF data, extrapolating the LF down to various limiting magnitudes, where they considered various constant values of $f_{\rm esc}$ and a redshift-dependent escape fraction. Our reionization history is more extended than these works, where the difference comes from low-luminosity galaxies contributing more at higher redshifts. Their resulting τ_e is still consistent with the latest WMAP and Planck data but on the low-end of the 1-σ errors. Our reionisation model uses a similar approach as Alvarez, Finlator & Trenti (2012) with $f_\star$ and $f_{\rm esc}$ being halo mass dependent, however, we use values that are calibrated from our simulation with six mass ranges instead of two. Their idea of a low-mass galaxy population driving early reionisation is plausible and is supported by our simulations. Like the aforementioned works, their reionisation history is slightly shorter than our results, mainly arising from their model only considering haloes with $M > 10^8 M_\odot$ as star-forming. The general trends, such as a peak in ionising emissivity and early-time and late-time asymptotes in the luminosity-averaged escape fraction, are found in our model, but clearly with different source parameters, the details have changed. Nevertheless, we find this type of reionisation history to be most plausible, considering the findings in our simulation presented in this paper.

5.4 Caveats

Our simulations include most of the relevant physical processes in galaxy formation and its associated star formation and feedback, but there are still some shortcomings in our work. The simulation volume is only 1 comoving Mpc^3, which misses the effects of large-scale reionisation and rare peaks in the cosmological density field. This, however, does not diminish our findings of the properties of early dwarf galaxies because stellar feedback is the dominant factor in simulating realistic galaxies (e.g. Wise et al. 2012a; Stinson et al. 2013; Hopkins et al. 2013). The small volume does restrict our analysis to 32 dwarf galaxies and evaluating the galaxy properties independent of time. The approach of combining the data at all outputs misses any evolution in the galaxy properties, but we have included the time-dependent effects of photo-suppression in our semi-analytic reionisation model.

We have not considered the effects of relative streaming velocities ($v_{\rm vel} \sim 30 \ {\rm km \, s^{-1}}$ at $z \sim 1100$) between baryons and DM that arise during recombination (Tseliakhovich & Hirata 2010). This phenomenon only suppresses Pop III star formation in the smallest minihaloes with $M \lesssim 10^6 M_\odot$ (Tseliakhovich, Barkana

& Hirata 2011; Greif et al. 2011b; Naoz, Yoshida & Gnedin 2012; O'Leary & McQuinn 2012) and should not significantly change our results because the circular velocities of the galaxy host haloes are much larger than the streaming velocity at $z < 20$.

On the topic of the escape fraction, there are a few processes that we do not model. First, we cannot capture the possibility of runaway massive stars that may boost $f_{\rm esc}$ as these stars travel into the outskirts of the dwarf galaxy and into the IGM (Conroy & Kratter 2012) because we model metal-enriched star formation at the stellar cluster scale. Second, we do not include the partial ionisation by X-ray radiation from X-ray binaries (McQuinn 2012; Power et al. 2013; Fragos et al. 2013) or mini-quasars (e.g Ricotti & Ostriker 2004b; Kuhlen & Madau 2005; Holley-Bockelmann, Wise & Sinha 2012; Grissom, Ballantyne & Wise 2014), which may contribute up to 10 per cent of the optical depth to Thomson scattering. Finally, we consider a Salpeter IMF ($dN/dM_\star \propto M_\star^\alpha$ with $\alpha = -2.35$) for metal-enriched stars, whereas recent observations of ultra-faint dwarf galaxies have suggested that the IMF slope is more shallow at $\alpha = 1.2^{+0.4}_{-0.5}$ for Hercules and $\alpha = 1.3 \pm 0.8$ for Leo IV (Geha et al. 2013). The shallower slope implies that their progenitors hosted star formation that favors massive stars more than present-day star formation. Wise & Cen (2009) also found that a top-heavy IMF increases the escape fraction by $\Delta f_{\rm esc} = 0.27 \pm 0.17$ but also suppresses star formation by $\sim$25 per cent in the H_2-cooling haloes. Considering a shallower IMF may change our results slightly in the low-mass end that we investigated, but it is still uncertain under which conditions the IMF becomes more top-heavy (e.g., see differing results in Jappsen et al. 2009; Smith et al. 2009; Safranek-Shrader, Milosavljević & Bromm 2014). On a similar topic, we used a characteristic mass of $100 M_\odot$ for our Pop III IMF, which is somewhat higher than recent Pop III star formation simulations that find characteristic masses around tens of $M_\odot$ (Turk, Abel & O'Shea 2009; Stacy, Greif & Bromm 2010; Greif et al. 2011a, 2012; Susa 2013). However, a recent paper by Hirano et al. (2014) studied 100 instances of Pop III protostar evolution with axisymmetric radiation hydrodynamics simulations that were initialised from a cosmological simulation. They found a wide range of possible stellar masses $M_\star = 10 - 1000 M_\odot$, and under this scenario, our choice of a Pop III IMF would still be within the uncertainties gathered from such simulations.

6 CONCLUSIONS

We present the characteristic properties and abundances of dwarf galaxies at high-redshift and their absolute contribution to cosmic reionisation. To obtain our results, we use a cosmological radiation hydrodynamics simulation that considers Pop II and III star formation with a self-consistent transition with their radiative feedback modeled with the radiation transport module ENZO+MORAY. In a previous paper (W12), we showed that the star formation history and stellar population of the most massive dwarf galaxy in the simulation analysed here agreed with the local dwarf galaxy metallicity-luminosity relation. We have further analysed this simulation that captures the buildup of the first galaxies, starting with their Pop III progenitors, focusing on their global properties, LF, UV escape fraction, and role during reionisation, and the highlights of our work are as follows:

(i) Low-luminosity galaxies with stellar masses up to $3 \times 10^4 M_\odot$, SFRs of $10^{-3} \ {\rm M_\odot \, yr^{-1}}$, and absolute UV magnitudes of -10 are able to form in H_2-cooling haloes ($T_{\rm vir} \leqslant 10^4$ K). This usually occurs in one burst, which then suppresses any further star

formation through stellar feedback, and star formation will recommence after sufficient gas has (re-)accreted into the potential well.

(ii) Gas fractions in the H_2-cooling haloes have a large spread and are, on average, $\sim$5–7 per cent, where $\sim$0.3–3 per cent of this gas form stars. In addition to internal suppression, they are subsequently photo-suppressed by an external radiation field.

(iii) The early dwarf galaxy LF flattens to $\sim$3 mag^{-1} Mpc^{-3} at $M_{UV} \gtrsim -12$. The galaxies in this plateau form in H_2-cooling haloes usually with one star formation event that produces an initial magnitude around $M_{UV} = -12$ and then increases as the stellar population ages.

(iv) The luminosity-weighted escape fraction decreases with halo mass with $f_{esc} \simeq 0.5$ in haloes with $M \leqslant 2 \times 10^7 M_\odot$, $f_{esc} \simeq 0.3$ in haloes with $2 \times 10^7 \leqslant M/M_\odot \leqslant 2 \times 10^8$, and $f_{esc} \simeq 0.05$ in larger haloes. The escape fraction is highly time dependent and is correlated with the SFR with an average delay of $\sim$10 Myr.

(v) The amount of ionising photons per unit mass escaping from the halo, i.e. $f_{esc} f_\star f_{gas}$, shows little evolution with halo mass with a mean value of $10^{-3.6}$ over the mass range captured in our simulation.

(vi) Low-luminosity galaxies hosted in H_2-cooling haloes propel the early epochs of reionisation, providing 75 per cent of the instantaneous emissivity at $z = 14$ when our reionisation model has an ionisation fraction of 20 per cent. These faintest galaxies contribute nearly 30 per cent of the ionising photon budget by $z = 6$.

(vii) Photo-suppression of low-luminosity galaxies leads to a photon-starved reionisation scenario by $z = 6$, agreeing with emissivities inferred from Lyα forest observations. By utilizing calibrated galaxy properties in our reionisation model, we obtain an optical depth to Thomson scattering $\tau_e = 0.093$, agreeing with the latest WMAP and Planck results.

(viii) The luminosity-weighted escape fraction and host halo mass smoothly decline and increase, respectively, with time, and we have given functional fits (Equations 17 and 18) to these trends for use in future studies.

We have shown that the faintest galaxies contribute a significant amount to the ionising photon budget during cosmic reionisation. Their consideration in reionisation calculations is essential in order to adhere to observational constrains, such as τ_e, the duration of reionisation, a mostly ionised IGM by $z \sim 6$, and the ionisation background at $z = 4 - 6$. We are currently following up this study with a larger dataset with more massive galaxies (Xu, Wise & Norman 2013) to further constrain galaxy scaling relations and galaxy observables during reionisation, which is timely with the future launch of JWST and commissioning of 30-m class ground-based telescopes.

REFERENCES

Abel T., Anninos P., Zhang Y., Norman M. L., 1997, New Astronomy, 2, 181
Abel T., Wandelt B. D., 2002, MNRAS, 330, L53
Ahn K., Iliev I. T., Shapiro P. R., Mellema G., Koda J., Mao Y., 2012, ApJL, 756, L16
Alvarez M. A., Finlator K., Trenti M., 2012, ApJL, 759, L38
Anninos P., Zhang Y., Abel T., Norman M. L., 1997, New Astronomy, 2, 209
Becker G. D., Bolton J. S., 2013, ArXiv e-prints (1307.2259)
Beckwith S. V. W. et al., 2006, AJ, 132, 1729
Benson A., Venkatesan A., Shull J. M., 2013, ApJ, 770, 76
Bertschinger E., 2001, ApJS, 137, 1
Biffi V., Maio U., 2013, MNRAS, 436, 1621
Bolton J. S., Haehnelt M. G., 2007, MNRAS, 382, 325
Bouwens R. J. et al., 2012a, ArXiv e-prints (1211.2230)
—, 2011, ApJ, 737, 90
—, 2012b, ApJL, 752, L5
Bradley L. D. et al., 2012, ApJ, 760, 108
—, 2013, ArXiv e-prints (1308.1692)
Bruzual G., Charlot S., 2003, MNRAS, 344, 1000
Bryan G. L., Norman M. L., 1997, ArXiv e-prints (astro-ph/9710187)
Bryan G. L., Norman M. L., Stone J. M., Cen R., Ostriker J. P., 1995, Computer Physics Communications, 89, 149
Cen R., Ostriker J. P., 1992, ApJL, 399, L113
Ciardi B., Bianchi S., Ferrara A., 2002, MNRAS, 331, 463
Ciardi B., Ferrara A., White S. D. M., 2003, MNRAS, 344, L7
Clarke C., Oey M. S., 2002, MNRAS, 337, 1299
Conroy C., Kratter K. M., 2012, ApJ, 755, 123
Couchman H. M. P., 1991, ApJL, 368, L23
Dijkstra M., Haiman Z., Rees M. J., Weinberg D. H., 2004, ApJ, 601, 666
Dijkstra M., Wyithe J. S. B., 2010, MNRAS, 408, 352
Dove J. B., Shull J. M., Ferrara A., 2000, ApJ, 531, 846
Efstathiou G., 1992, MNRAS, 256, 43P
Efstathiou G., Davis M., White S. D. M., Frenk C. S., 1985, ApJS, 57, 241
Emberson J. D., Thomas R. M., Alvarez M. A., 2013, ApJ, 763, 146
Fan X., Narayanan V. K., Strauss M. A., White R. L., Becker R. H., Pentericci L., Rix H.-W., 2002, AJ, 123, 1247
Fan X. et al., 2006, AJ, 132, 117
Fernandez E. R., Shull J. M., 2011, ApJ, 731, 20
Ferrara A., Loeb A., 2013, MNRAS, 431, 2826
Finkelstein S. L. et al., 2012, ApJ, 758, 93
Finlator K., Davé R., Özel F., 2011, ApJ, 743, 169
Finlator K., Oh S. P., Özel F., Davé R., 2012, MNRAS, 427, 2464
Fragos T., Lehmer B. D., Naoz S., Zezas A., Basu-Zych A., 2013, ApJL, 776, L31
Fujita A., Martin C. L., Mac Low M.-M., Abel T., 2003, ApJ, 599, 50
Furlanetto S. R., Zaldarriaga M., Hernquist L., 2004, ApJ, 613, 1
Geha M. et al., 2013, ApJ, 771, 29
Glover S. C. O., Abel T., 2008, MNRAS, 388, 1627
Gnedin N. Y., 2000, ApJ, 542, 535
—, 2008, ApJL, 673, L1
Gnedin N. Y., Hui L., 1998, MNRAS, 296, 44
Gnedin N. Y., Kravtsov A. V., Chen H.-W., 2008, ApJ, 672, 765
Gnedin N. Y., Ostriker J. P., 1997, ApJ, 486, 581
Górski K. M., Hivon E., Banday A. J., Wandelt B. D., Hansen

F. K., Reinecke M., Bartelmann M., 2005, ApJ, 622, 759

Greif T. H., Bromm V., 2006, MNRAS, 373, 128

Greif T. H., Bromm V., Clark P. C., Glover S. C. O., Smith R. J., Klessen R. S., Yoshida N., Springel V., 2012, MNRAS, 424, 399

Greif T. H., Glover S. C. O., Bromm V., Klessen R. S., 2010, ApJ, 716, 510

Greif T. H., Springel V., White S. D. M., Glover S. C. O., Clark P. C., Smith R. J., Klessen R. S., Bromm V., 2011a, ApJ, 737, 75

Greif T. H., White S. D. M., Klessen R. S., Springel V., 2011b, ApJ, 736, 147

Grissom R. L., Ballantyne D. R., Wise J. H., 2014, A&A, 561, A90

Grogin N. A. et al., 2011, ApJS, 197, 35

Gunn J. E., Peterson B. A., 1965, ApJ, 142, 1633

Haardt F., Madau P., 2012, ApJ, 746, 125

Haiman Z., Abel T., Rees M. J., 2000, ApJ, 534, 11

Haiman Z., Rees M. J., Loeb A., 1997, ApJ, 476, 458

Heger A., Fryer C. L., Woosley S. E., Langer N., Hartmann D. H., 2003, ApJ, 591, 288

Hirano S., Hosokawa T., Yoshida N., Umeda H., Omukai K., Chiaki G., Yorke H. W., 2014, ApJ, 781, 60

Holley-Bockelmann K., Wise J. H., Sinha M., 2012, ApJL, 761, L8

Hopkins P. F., Keres D., Onorbe J., Faucher-Giguere C.-A., Quataert E., Murray N., Bullock J. S., 2013, ArXiv e-prints (1311.2073)

Iliev I. T., Mellema G., Ahn K., Shapiro P. R., Mao Y., Pen U.-L., 2013, ArXiv e-prints (1310.7463)

Iliev I. T., Mellema G., Pen U., Merz H., Shapiro P. R., Alvarez M. A., 2006, MNRAS, 369, 1625

Inoue A. K., Iwata I., 2008, MNRAS, 387, 1681

Iwata I. et al., 2009, ApJ, 692, 1287

Jappsen A.-K., Klessen R. S., Glover S. C. O., Mac Low M.-M., 2009, ApJ, 696, 1065

Johnson J. L., Bromm V., 2006, MNRAS, 366, 247

Johnson J. L., Dalla V. C., Khochfar S., 2013, MNRAS, 428, 1857

Johnson J. L., Greif T. H., Bromm V., 2008, MNRAS, 388, 26

Johnson J. L., Greif T. H., Bromm V., Klessen R. S., Ippolito J., 2009, MNRAS, 399, 37

Jones T. A., Ellis R. S., Schenker M. A., Stark D. P., 2013, ApJ, 779, 52

Koekemoer A. M. et al., 2013, ApJS, 209, 3

—, 2011, ApJS, 197, 36

Komatsu E., et al., 2011, ApJS, 192, 18

Kuhlen M., Faucher-Giguère C.-A., 2012, MNRAS, 423, 862

Kuhlen M., Madau P., 2005, MNRAS, 363, 1069

Machacek M. E., Bryan G. L., Abel T., 2001, ApJ, 548, 509

Madau P., Haardt F., Rees M. J., 1999, ApJ, 514, 648

Maio U., Ciardi B., Dolag K., Tornatore L., Khochfar S., 2010, MNRAS, 407, 1003

McQuinn M., 2012, MNRAS, 426, 1349

McQuinn M., Oh S. P., Faucher-Giguère C.-A., 2011, ApJ, 743, 82

Mitra S., Ferrara A., Choudhury T. R., 2013, MNRAS, 428, L1

Mo H. J., White S. D. M., 2002, MNRAS, 336, 112

Mortlock D. J. et al., 2011, Nature, 474, 616

Muratov A. L., Gnedin O. Y., Gnedin N. Y., Zemp M., 2013, ApJ, 772, 106

Naoz S., Yoshida N., Gnedin N. Y., 2012, ApJ, 747, 128

Nestor D. B., Shapley A. E., Steidel C. C., Siana B., 2011, ApJ, 736, 18

Nomoto K., Tominaga N., Umeda H., Kobayashi C., Maeda K., 2006, Nuclear Physics A, 777, 424

Oesch P. A. et al., 2012, ApJ, 759, 135

—, 2013, ApJ, 773, 75

Okamoto T., Gao L., Theuns T., 2008, MNRAS, 390, 920

O'Leary R. M., McQuinn M., 2012, ApJ, 760, 4

O'Shea B. W., Norman M. L., 2008, ApJ, 673, 14

Paardekooper J.-P., Khochfar S., Dalla Vecchia C., 2013, MNRAS, 429, L94

Paardekooper J.-P., Pelupessy F. I., Altay G., Kruip C. J. H., 2011, A&A, 530, A87

Pawlik A. H., Milosavljević M., Bromm V., 2013, ApJ, 767, 59

Pawlik A. H., Schaye J., van Scherpenzeel E., 2009, MNRAS, 394, 1812

Planck Collaboration et al., 2013, ArXiv e-prints (1303.5076)

Postman M. et al., 2012, ApJS, 199, 25

Power C., James G., Combet C., Wynn G., 2013, ApJ, 764, 76

Press W. H., Schechter P., 1974, ApJ, 187, 425

Razoumov A. O., Sommer-Larsen J., 2006, ApJL, 651, L89

—, 2007, ApJ, 668, 674

—, 2010, ApJ, 710, 1239

Ricotti M., Gnedin N. Y., 2005, ApJ, 629, 259

Ricotti M., Gnedin N. Y., Shull J. M., 2008, ApJ, 685, 21

Ricotti M., Ostriker J. P., 2004a, MNRAS, 350, 539

—, 2004b, MNRAS, 352, 547

Ricotti M., Shull J. M., 2000, ApJ, 542, 548

Ritter J. S., Safranek-Shrader C., Gnat O., Milosavljević M., Bromm V., 2012, ApJ, 761, 56

Robertson B. E., Ellis R. S., Dunlop J. S., McLure R. J., Stark D. P., 2010, Nature, 468, 49

Robertson B. E. et al., 2013, ApJ, 768, 71

Safranek-Shrader C., Agarwal M., Federrath C., Dubey A., Milosavljević M., Bromm V., 2012, MNRAS, 426, 1159

Safranek-Shrader C., Milosavljević M., Bromm V., 2014, MNRAS

Schaerer D., 2002, A&A, 382, 28

—, 2003, A&A, 397, 527

Shapiro P. R., 1986, PASP, 98, 1014

Shapiro P. R., Giroux M. L., 1987, ApJL, 321, L107

Shapiro P. R., Iliev I. T., Raga A. C., 2004, MNRAS, 348, 753

Shapley A. E., Steidel C. C., Pettini M., Adelberger K. L., Erb D. K., 2006, ApJ, 651, 688

Sheth R. K., Mo H. J., Tormen G., 2001, MNRAS, 323, 1

Shull J. M., Harness A., Trenti M., Smith B. D., 2012, ApJ, 747, 100

Smith B., Sigurdsson S., Abel T., 2008, MNRAS, 385, 1443

Smith B. D., Turk M. J., Sigurdsson S., O'Shea B. W., Norman M. L., 2009, ApJ, 691, 441

So G. C., Norman M. L., Reynolds D. R., Harkness R. P., 2013, ArXiv e-prints (1311.2152)

Sobacchi E., Mesinger A., 2013, MNRAS, 432, 3340

Sokasian A., Abel T., Hernquist L., Springel V., 2003, MNRAS, 344, 607

Stacy A., Greif T. H., Bromm V., 2010, MNRAS, 403, 45

Steidel C. C., Pettini M., Adelberger K. L., 2001, ApJ, 546, 665

Stinson G. S., Brook C., Macciò A. V., Wadsley J., Quinn T. R., Couchman H. M. P., 2013, MNRAS, 428, 129

Susa H., 2013, ApJ, 773, 185

The Enzo Collaboration et al., 2013, ArXiv e-prints (1307.2265)

Thoul A. A., Weinberg D. H., 1996, ApJ, 465, 608

Trac H., Cen R., 2007, ApJ, 671, 1

Trac H. Y., Gnedin N. Y., 2011, Advanced Science Letters, 4, 228

Truelove J. K., Klein R. I., McKee C. F., Holliman, II J. H., Howell L. H., Greenough J. A., 1997, ApJL, 489, L179+

Tseliakhovich D., Barkana R., Hirata C. M., 2011, MNRAS, 1501

Tseliakhovich D., Hirata C., 2010, Phys. Rev. D, 82, 083520

Tumlinson J., Shull J. M., 2000, ApJL, 528, L65

Turk M. J., Abel T., O'Shea B., 2009, Science, 325, 601

Turk M. J., Smith B. D., Oishi J. S., Skory S., Skillman S. W., Abel T., Norman M. L., 2011, ApJS, 192, 9

Vanzella E. et al., 2012, ApJ, 751, 70

Verhamme A., Schaerer D., Atek H., Tapken C., 2008, A&A, 491, 89

Verhamme A., Schaerer D., Maselli A., 2006, A&A, 460, 397

Verner D. A., Ferland G. J., Korista K. T., Yakovlev D. G., 1996, ApJ, 465, 487

Warren M. S., Abazajian K., Holz D. E., Teodoro L., 2006, ApJ, 646, 881

Whalen D., van Veelen B., O'Shea B. W., Norman M. L., 2008, ApJ, 682, 49

Willman B., Strader J., 2012, AJ, 144, 76

Willott C. J. et al., 2007, AJ, 134, 2435

—, 2010, AJ, 139, 906

Wise J. H., Abel T., 2007, ApJ, 671, 1559

—, 2008a, ApJ, 684, 1

—, 2008b, ApJ, 685, 40

—, 2011, MNRAS, 414, 3458

Wise J. H., Abel T., Turk M. J., Norman M. L., Smith B. D., 2012a, MNRAS, 427, 311

Wise J. H., Cen R., 2009, ApJ, 693, 984

Wise J. H., Turk M. J., Norman M. L., Abel T., 2012b, ApJ, 745, 50

Woo J., Courteau S., Dekel A., 2008, MNRAS, 390, 1453

Wood K., Loeb A., 2000, ApJ, 545, 86

Woodward P., Colella P., 1984, Journal of Computational Physics, 54, 115

Xu H., Wise J. H., Norman M. L., 2013, ApJ, 773, 83

Yajima H., Choi J.-H., Nagamine K., 2011, MNRAS, 412, 411

Zackrisson E. et al., 2012, MNRAS, 427, 2212

Zahn O., Mesinger A., McQuinn M., Trac H., Cen R., Hernquist L. E., 2011, MNRAS, 414, 727

Zahn O. et al., 2012, ApJ, 756, 65

This paper has been typeset from a TeX/ LaTeX file prepared by the author.